Optical properties of novel semiconductor nanostructures: wurtzite InP/InAs/InP core-multishell nanowires

Ken Goto

(Doctoral Program in Frontier Science)

Submitted to the Graduate School of

Pure and Applied Sciences

in Partial Fulfillment of the Requirements

for the Degree of Doctor of Philosophy in

Science

at the

University of Tsukuba

ABSTRACT

Core-multishell nanowire (CMS-NW) is a new class of nanowire containing quantum well and quantum wire structures. It shows bright luminescence, applicable to photonic devices. CMS-NW has advantages over the carbon nanotube in terms of the selectivity of the composition materials and in the formation of heterojunctions. Much effort has been devoted to growth and fabrication of CMS-NW structures. However, there is very little information on the electronic structure and optical properties of this new class of structures. We study optical transitions from a periodic array of InP/InAs/InP CMS-NWs having a wurtzite crystal structure by using photoluminescence (PL) spectroscopy, PL excitation (PLE) spectroscopy, and time-resolved (TR) PL spectroscopy.

Multiple peaks appeared in the PL spectra owing to the monolayer variation of InAs layers. Observing a large Stokes shift between PL and PLE spectra and a slow and nonexponential decay of PL with an effective decay time of 16 ns suggest a type-II band alignment. Band-offset calculation based on the "model-solid theory" supports the type-II band lineup if the InAs layer in the wurtzite CMS-NW is assumed to be placed in three-dimensional compressive strain.

Each PL peak has a broad PL band coming from the inhomogeneous broadening in a core-multishell single nanowire. Inhomogeneous broadening causes time-dependent spectral red shift (spectral diffusion) at a constant energy-loss rate. The TR-PL measurement using the time-correlated single photon counting (TCSPC) technique clarifies that spectral diffusion takes place in two stages (initially at a rate of -1.98×10^6 eV/s and later at a rate of -0.3×10^6 eV/s). The first one is ascribed to spectral diffusion on the side plane in the nanowire and the second one is ascribed to spectral diffusion at the corner line in the nanowire. This suggests that photo-excited excitons in a CMS-NW move from the side plane in the nanowire toward the corner line in the nanowire. The difference between the exciton confinement energy in the side plane in the CMS-NW and the corner line in the CMS-NW, calculated by the finite-element-method, agrees with the difference between energies from which the two-dimensional spectral diffusion and the one-dimensional spectral diffusion start. This suggests the exciton movement from the side plane toward the corner line in the

CMS-NW.

The PL peak shows a blue shift with a cube-root dependence on the excitation power. This blue shift results from the band bending in the type-II band configuration. The self-consistent solution of the electron confinement energy derived from Poisson and Schrödinger equations demonstrates its blue shift with a cube-root dependence on the excitation power. Fast decay caused by the relaxation of the band bending is observed at higher energy sides of the PL bands in the TR-PL measurement. The examination of the exciton density clarifies that the exciton diffusion takes place in the CMS-NW within initial 1 ns. Good agreement between the experimental temporal change of the exciton density and the simulated one is obtained.

CONTENTS

Chapter 1.

Introduction

1.1 Background

Semiconductor nanowires (NWs) can act as waveguide for light as well as for charge carriers. Thus, they have the potential to work as both the active device element and the interconnects for the integrated electronic and photonic circuits **[1.1]**. The possibility of layer-by-layer assembly of NW building blocks is promising for three-dimensional integrated electronics **[1.2]**. Several nanoelectronic and photonic devices, including lasers **[1.3]**, polarization sensitive photodetectors **[1.4]**, and field-effect transistors **[1.5]** have been fabricated by using NWs. Incorporation of heterostructures into a NW can enhance its capability for multifunctional devices. Axial heterostructured NWs have been used to fabricate single photon emitters **[1.6]**, single electron transistors **[1.7]** etc. Introduction of radial heterostructures by forming core-shell and core-multishell structures has additional benefits. It passivates the surface states and helps to improve the optical cavity properties. Possible strain effects between lattice mismatched core and shell offer flexibility in band structure engineering.

Core-multishell nanowire (CMS-NW) is a new class of nanowire containing quantum well (QW) and quantum wire (QWR) structures. It shows bright luminescence because the active layer is covered with shell. CMS-NW has advantages over the carbon nanotube in terms of the selectivity of the composition materials and in the formation of heterojunctions. The core-and shell layers can enhance confinement of both carriers and photons in the active layer. Therefore the CMS-NWs are applicable to photonic devices **[1.8, 1.9]**. Much effort has been devoted to growth and fabrication of CMS-NW structures and the periodic arrays of such structures **[1.10, 1.11]**. However, there is very little information on the electronic structure and optical properties of this new class of structures. Information is even less when the active layer becomes ultrathin.

InAs is interesting material for applications because of the narrow band gap in the near-infrared at the telecommunication wavelength (1.3 μm and 1.55 μm). Moreover, InAs has small effective mass and high electron mobility which are indispensable properties for applying to low power and ultra high-speed devices. Crystal structure of

bulk InAs is zincblende. Crystal structure of InAs QWs (for example, InAs/InP QW) is zincblende, too. However, the crystal structures of InAs nanowires **[1.12]**, $InAs_{1-x}P_x$ nanowires **[1.13]**, and also for core-shell structures of InAs/InP **[1.14, 1.15]** are wurtzite. Information on wurtzite InAs is very rare. Therefore, it is important in the application to understand electrical and optical properties of wurtzite InP/InAs/InP CMS-NWs.

1.2 Previous studies on wurtzite InP/InAs nanowires and core-multishell nanowires

So far, wurtzite InP/InAs nanowires are mainly studied on applicative properties such as *I-V* characteristic **[1.13, 1.16-1.18]** and band gap energy **[1.18-1.21]**. Measurement of the *I-V* characteristic clarifies that the InP/InAs nanowires exhibits good ohmic characteristic and the resistance is found to decrease with the increase in temperature **[1.13, 1.16]**. Moreover, very high electron mobility of an InP/InAs nanowire (11500 cm^2/Vs) compared with a carbon nanotube (~1000 cm^2/Vs) was observed **[1.17]**. This promises the application to a high-performance device. On the other hand, the band gap energy is investigated both experimentally **[1.18, 1.19]** and theoretically **[1.20, 1.21]**. It is confirmed that the band gap energy is found to decrease with the increase in wire thickness due to quantum confinement in the plane perpendicular to the nanowire axis **[1.18, 1.20]**. In addition, the band gap energy is reported to increase due to the strain by calculations based on six-band strain-dependent $k \cdot p$ theory **[1.21]**. However, little is known about electrical and optical properties of wurtzite InP/InAs heterostructures. Especially, there is no report on the observation of the type-II behavior.

In addition, there are little reports on fundamental optical properties of CMS-NW. Several studies have been made on the fabrication procedures **[1.8, 1.10, 1.11]**. III-V compound semiconductor CMS-NW functioned as a wavelength-controlled lasers **[1.22]** and light-emitting diodes **[1.8]** are investigated. It is applied to attractive building blocks for active photonic devices. Moreover, Aharonov-Bohm effect is reported in CMS-NW **[1.23]**. However, little attention has been given to the fundamental optical properties of CMS-NW. There have been no studies time-resolved photoluminescence spectroscopy in CMS-NW.

1.3 Our study

We investigate optical properties of InP/InAs/InP CMS-NWs by using spectrally-resolved photoluminescence (PL) and PL excitation (PLE) and time-resolved (TR) spectroscopy. InP/InAs/InP CMS-NWs consist of an ultrathin InAs layer, and an InP core and an InP outer shell with the wider band-gap. They have wurtzite structure with cross-sectional hexagonal symmetry and translational symmetry along the wire **[1.10]**. The buried InAs layer acts as strained quantum well and wire.

The PL spectrum has multiple peaks due to the monolayer (ML) scale variation of the InAs layer. Inhomogeneous broadening arises in this sample due to short range interface nanoroughness and As-P intermixing at the interface. Disorder induced potential fluctuation causes exciton localization. A large Stokes shift between PL and PLE spectra is observed, which suggests type-II radiative recombination along with the absence of strong PLE peak. With increasing excitation power (P) the PL peaks show a blueshift with cube-root dependence on P, supporting type-II radiative transition. We can explain the blueshift by using a band bending model.

Transient processes of excitons in InP/InAs/InP CMS-NWs were studied by TR-PL measurements. We examined the TR-PL in two time regions, thousand picosecond region by using a streak camera and hundred nanosecond region by using a timecorrelated single photon counting (TCSPC) technique, respectively. Temporal change of the PL peak intensity shows a slow and nonexponential decay of PL with an effective decay time of 16 ns, as is consistent with type-II optical transitions. Fast spectral decay is present at the higher energy side of the PL band. The band bending in the type-II system explains the fast decay on a carrier diffusion model. Average energy of the PL band shows a spectral diffusion in both QW and QWR of the InP/InAs/InP CMS-NW.

References

[1.1] D. J. Sirbuly, M. Law, H. Yan, and P. Yang: J. Phys. Chem. B **109**, 15190 (2005).

[1.2] A. Javey, S. Nam, R. S. Friedman, H. Yan, and C. M. Lieber: Nano Lett. **7**, 773 (2007).

[1.3] M. H. Huang, S. Mao, H. Feick, H. Yan, Y. Wu, H. Kind, E. Weber, R. Russo, and P. Yang: Science **292**, 1897 (2001).

[1.4] J. Wang, M. S. Gudiksen, X. Duan, Y. Cui, and C. M. Lieber: Science **293**, 1455 (2001).

[1.5] B. K. Kim, J. J. Kim, J. O. Lee, K. J. Kong, H. J. Seo, and C. J. Lee: Phys. Rev. B **71**, 153313 (2005).

[1.6] M. T. Borgström, D. Bonacchi, L. Zobbi, F. M. Piras, E. A. Speets, A. Caneschi, A. Cornia, A. Magnani, B. J. Ravoo, D. N. Reinhoudt, R. Sessoli, and D. Gatteschi: Nano Lett. **5**, 1439 (2005).

[1.7] C. Thelander, T. Mårtensson, M. T. Björk, B. J. Ohlsson, M. W. Larsson, L. R. Wallenberg, and L. Samuelson: Appl. Phys. Lett. **83**, 2052 (2003).

[1.8]: L. J. Lauhon, M. S. Gudiksen, D. Wang, and C. M. Lieber: Nature **420**, 57 (2002).

[1.9]: F. Qian, S. Gradecak, Y. Li, C. Y. Wen, and C. M. Lieber: Nano Lett. **5**, 2287 (2005).

[1.10]: P. Mohan, J. Motohisa, and T. Fukui: Appl. Phys. Lett. **88**, 133105 (2006).

[1.11]: P. K. Mohseni, C. Maunders, G. A. Botton, and R. R. LaPierre: Nanotechnology **18**, 445304 (2007).

[1.12]: K. A. Dick, Z. Geretovszky, A. Mikkelsen, L. S. Karlsson, E. Lundgren, J.-O. Malm, J. N. Andersen, L. Samuelson, W. Seifert, B. A. Wacaser, and K. Deppert: Nanotechnology **17**, 1344 (2006).

[1.13]: A. I. Persson, M. T. Björk, S. Jeppesen, J. B. Wagner, L. R. Wallenberg, and L. Samuelson: Nano Lett. **6**, 403 (2006).

[1.14]: Z. Zanolli, L. E. Fröberg, M. T. Björk, M.-E. Pistol, and L. Samuelson: Thin Solid Films **515**, 793 (2006).

[1.15]: P. Mohan, J. Motohisa, and T. Fukui: Nanotechnology **16**, 2903 (2005).

[1.16]: P. Mohan, J. Motohisa, and T. Fukui: Appl. Phys. Lett. **88**, 013110 (2006).

[1.17]: X. Jiang, Q. Xiong, S. Nam, F. Qian, Y. Li, and C. M. Lieber: Nano Lett. **7**, 3214 (2007).

[1.18]: R. Agarwal: Small **4**, 1872 (2008).

[1.19]: J. Trägårdh, A. I. Persson, J. B. Wagner, D. Hessman and L. Samuelson: J. Appl. Phys. **101**, 123701 (2007).

[1.20]: Y- M. Niquet and D. C. Mojica: Phys. Rev. B **77**, 115316 (2008).

[1.21]: Z. Zanolli, M- E. Pistol, L. E. Fröberg and L. Samuelson: J. Phys.: Condens. Matter **19**, 295219 (2007).

[1.22]: F. Qian, Y. Li, S. Gradečak, H- G. Park, Y. Dong, Y. Ding, Z. L. Wang and C. M. Lieber: Nature Materials **7**, 701 (2008).

[1.23]: S. Nomura, K. Tsumura, P. Mohan, J. Motohisa and T. Fukui: Physica E **40**, 1081 (2008).

Chapter 2.

Experimental procedures

2.1 InP/InAs/InP core-multishell nanowires

The sample studied contains vertically oriented InP/InAs/InP CMS-NW hexagonal arrays with a 400 nm period, uniformly grown by using selective area metalorganic vapor phase epitaxy. **Figure 2.1 (a)** shows schematic images of the sample. 224 pieces of blocks are arranged in 14 × 16 matrix structure. The size of block is a square 50 × 50 μm^2 in area, and about 10,000 wires are contained in one block. **Figure**

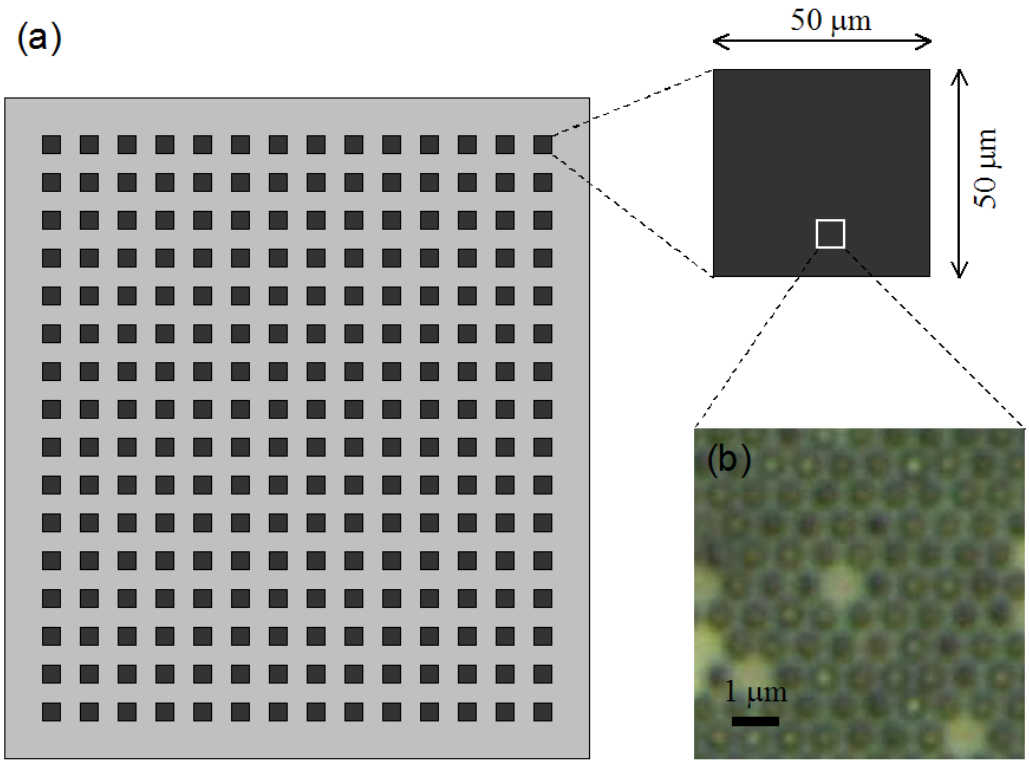

Figure 2.1 (a) Schematic images of sample component. (b) The microscopic image of InP/InAs/InP CMS-NWs.

2.1 (b) shows the top view image of the sample seen with an optical microscope. We can see the honeycomb-structure of the CMS-NW array. The length and the distance between opposite angles of the hexagonal pillar CMS-NW were 2 μm and 140 nm, respectively. Schematic images of the vertical and horizontal cross sections of the hexagonal pillar CMS-NW are shown in **Figure 2.2 (a)**. An InAs layer a few monolayers thick is embedded between an InP core and an outer shell.

The buried InAs layer forms a hexagonal tube. Since the sidewall of the hexagonal tube is formed in the quantum well (QW) structure, the InP/InAs/InP hetero structure, we consider that the CMS-NW is similar to QW. The optical properties of the QW are considered to dominate over those of the CMS-NW. On the other hand, the corner of the hexagonal tube is regarded as the V-shaped quantum wire (QWR) structure **[2.1]**. The CMS-NW consists of both QW and QWR. Because the CMS-NW consists of 6 QWs and 6 QWRs in hexagonal symmetry, we take an element, a QW structure and a QWR structure, from the CMS-NW and define the coordinates, as shown in **Figure 2.2 (b)**.

Transmission electron microscopy studies exhibit that both InP and InAs lattices have a wurtzite crystal structure in these CMS-NWs **[2.2,2.3]**. Since there is large lattice mismatch (over 4 %) between very thin wurtzite InAs and thick wurtzite InP, the buried InAs lattice is considered to be highly strained and to be equalized to the InP lattice. Further details of the sample structure, scanning electron microscopy images and growth procedure are shown in **Ref. 2.4**.

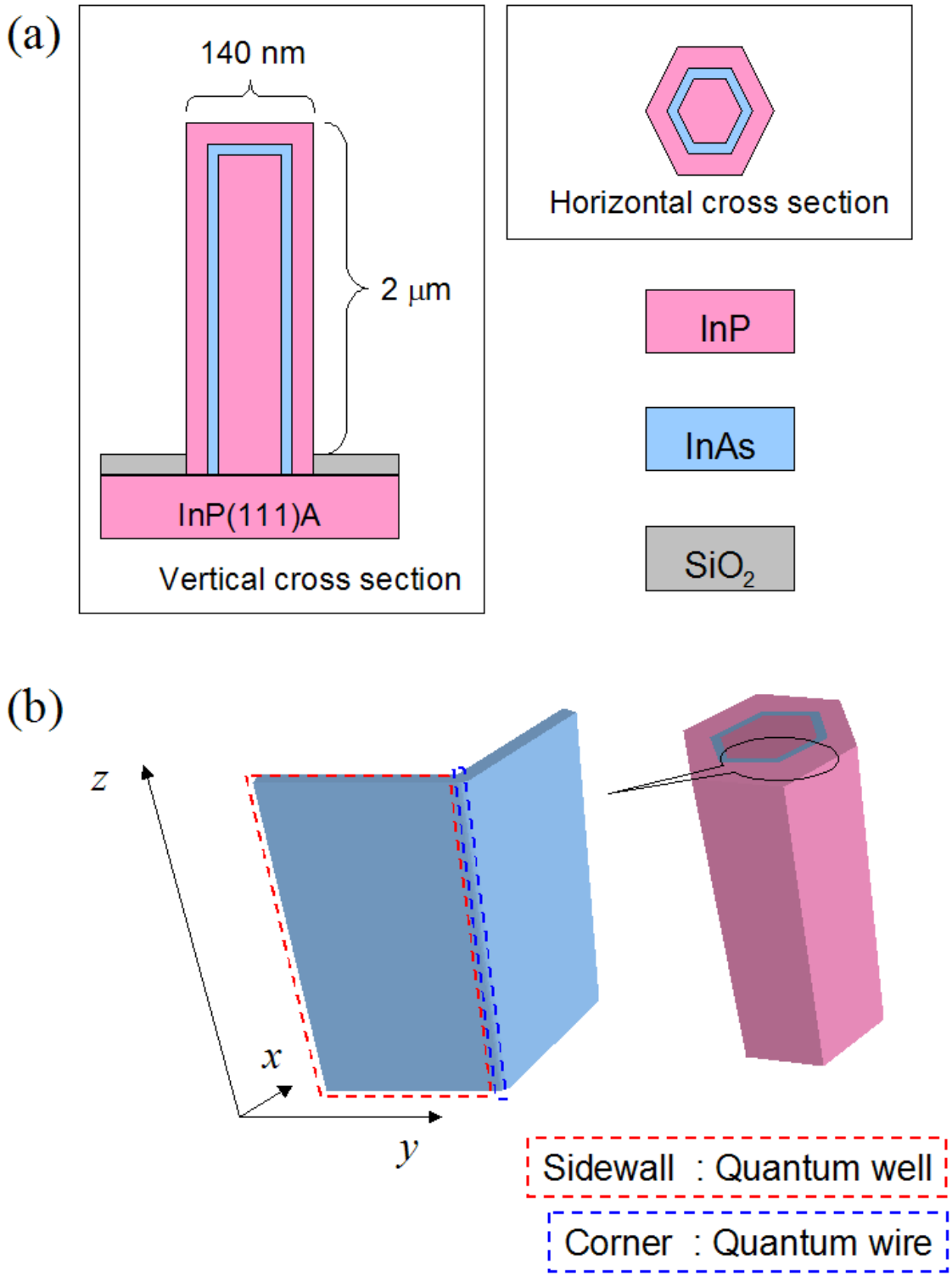

Figure 2.2 (a) Schematic images of the vertical and horizontal cross sections of the CMS-NW.
(b) The coordinates of the CMS-NW

2.2 Experimental details

Micro-photoluminescence measurement

The schematic illustration of micro-PL measurement system is shown in **Figure 2.3**. This system can select two kinds of the light sources. A halogen lamp was used to illuminate the sample and its image is measured by a CCD camera. A frequency-doubled Nd:YVO_4 laser (wavelength is 532 nm) is used for the light source of the micro-PL measurement. The sample was held in a liquid-helium continuous-flow optical cryostat at 5 K. The micro-PL signal was collected with a confocal microscope. The objective lens and the 1st imaging lens magnify the image of the sample on the pinhole by 30 times. The signal from a single CMS-NW passes through the pinhole 60 μm in diameter. The micro-PL passes through the optical fiber and is dispersed in a spectrometer with a focal length of 25 cm and is detected by a liquid-N_2-cooled charge-coupled device.

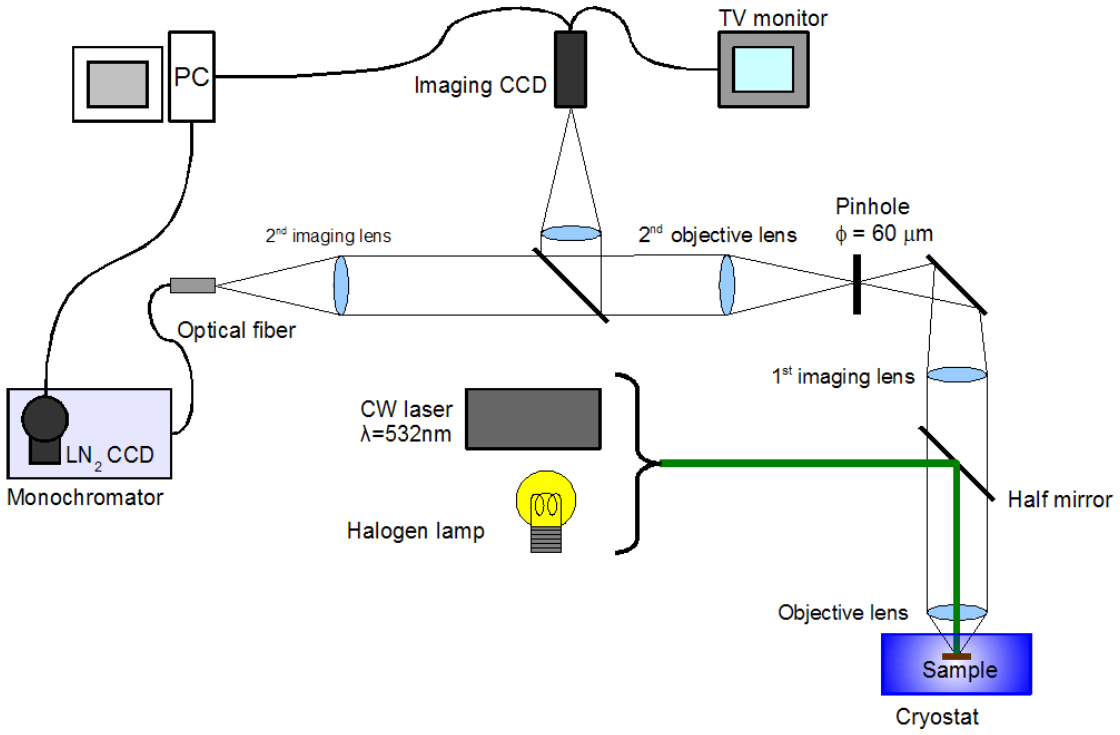

Figure 2.3 Micro-PL measurement system.

Photoluminescence and photoluminescence excitation measurements

The schematic set-up of PL and PLE measurements system is shown in **Figure 2.4**. The sample was held in a liquid-helium optical cryostat at 2 K. A tunable CW Ti:Sapphire laser was used for the excitaion. The PL signal was dispersed in a double monochromator (spectral resolution ~0.02 meV), and measured by a liquid N_2-cooled InGaAsP photomultiplier tube, and a photon counter. The PLE spectrum is measured by monitoring PL intensity.

Time-resolved photoluminescence measurement
(Streak camera)

The temporal change of PL spectra in the thousand picosecond time region is measured by using a synchroscan infrared streak camera with time resolution of 30 ps. The schematic illustration of streak camera measurement system is shown in **Figure 2.5**. The light source is a femtosecond mode-locked Ti:sapphire laser operating at the photon

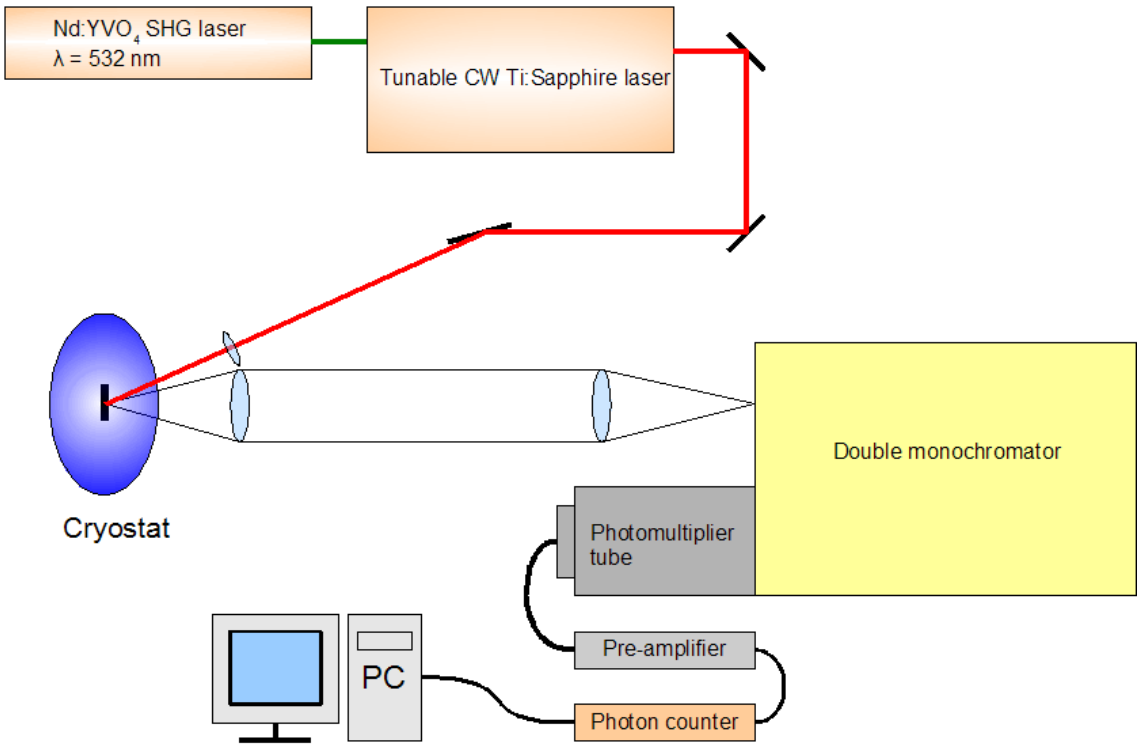

Figure 2.4 PL and PLE measurement system.

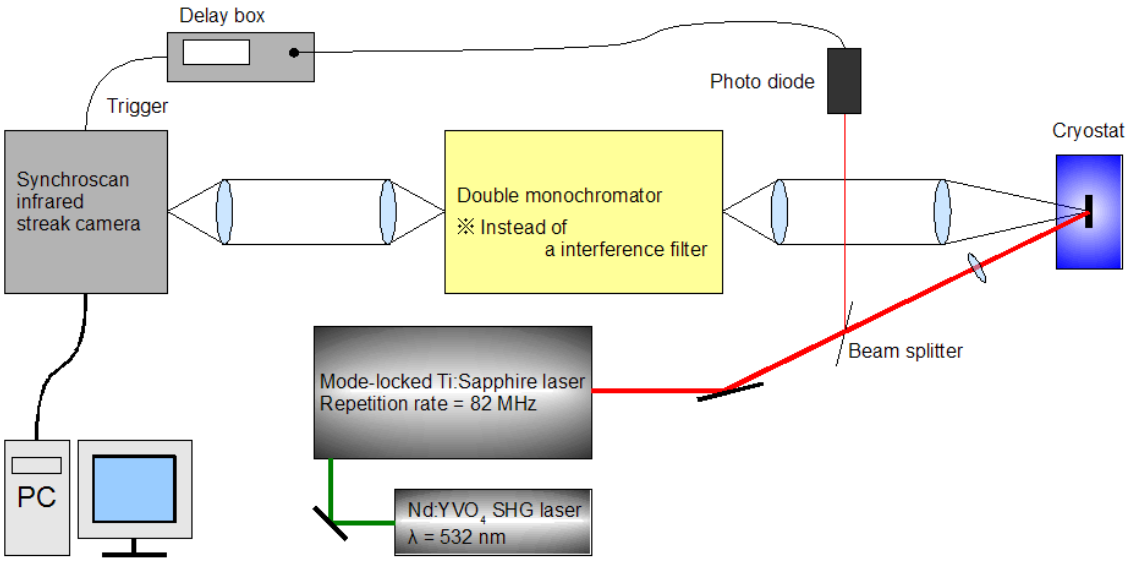

Figure 2.5 TR-PL measurement system by using a streak camera.

energy of 1.38 eV, below the InP barrier band-gap energy, at an 82 MHz repetition rate. A double monochromator is set up instead of a interference filter, to choose a spectral band in PL.

Time-resolved photoluminescence measurement
(Time-correlated single photon counting)

The temporal change of PL spectra in the hundred nanosecond time region is measured by means of standard TCSPC technique. The schematic illustration of a TCSPC measurement system is shown in **Figure 2.6**. The light source is a picosecond mode-locked Ti:sapphire laser operating at the photon energy of 1.38 eV, and we reduced the laser repetition rate to 820 kHz by using a pulse picker. An infrared photomultiplier with an InGaAsP target was used for the detection. The pulse from the photomultiplier was used to start a time-to-amplitude converter (TAC), and the pulse from the photodiode was used to stop the TAC through the delay device. The time resolution of our TCSPC system is 0.5 ns.

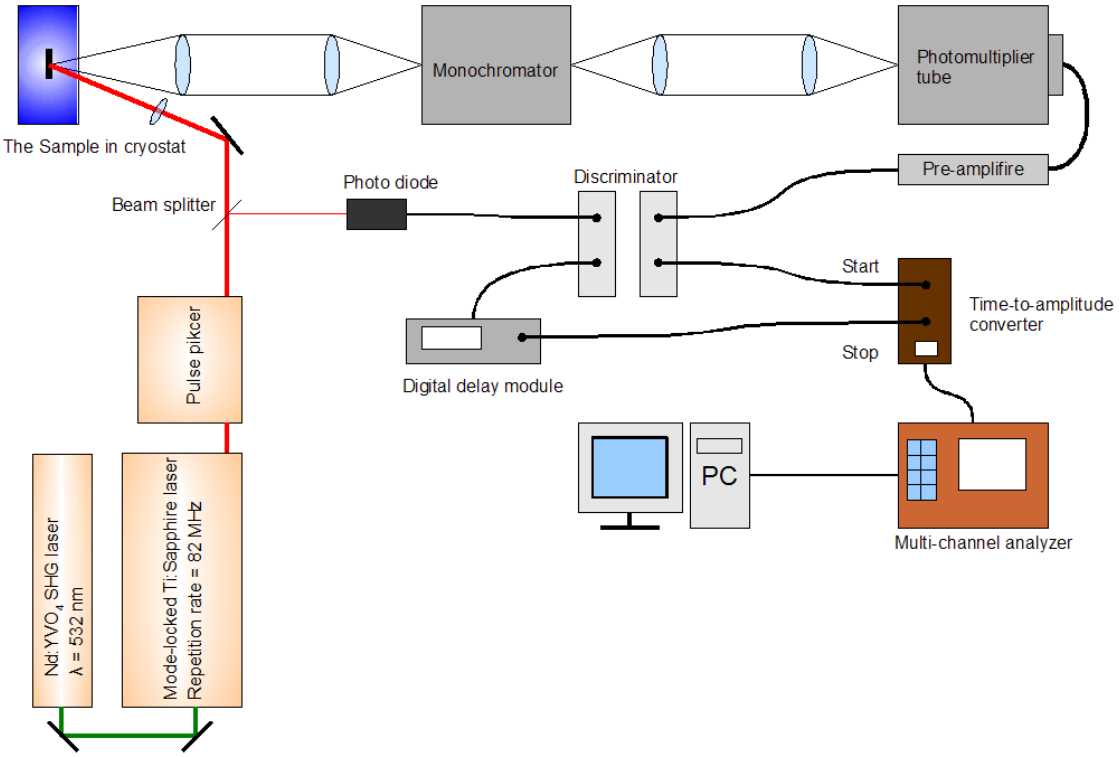

Figure 2.6 TR-PL measurement system by using time-correlated single photon counting.

References

[2.1]: X- L. Wang, V. Voliotis: J. Appl. Phys. **99**, 121301 (2006).
[2.2]: P. Mohan, J. Motohisa, and T. Fukui: Nanotechnology **16**, 2903 (2005).
[2.3]: P. Mohan, J. Motohisa, and T. Fukui: Appl. Phys. Lett. **88**, 013110 (2006).
[2.4]: P. Mohan, J. Motohisa, and T. Fukui: Appl. Phys. Lett. **88**, 133105 (2006).

Chapter 3.

Band line-up

3.1 Introduction

In this chapter we report band line-up studies on the periodic array of InP/InAs/InP CMS-NWs by using TR-PL and PLE measurements. Both InP and InAs have a wurtzite crystal structure in the NW form, although bulk InP and InAs crystallize to a zincblende structure. Moreover, in our CMS-NW sample a thin InAs layer is surrounded by thick InP layers from all sides and the InP layers act like a mold.

In the first approximation, we may consider that the InAs lattice experiences a three-dimensional compressive strain and attains the size of the InP lattice in all directions unlike InAs/InP QWs, where the InAs lattice is compressed in the crystal growth plane and is elongated in the growth direction. There have been a few studies on ultrathin InAs/InP QWs having zincblende structure **[3.1,3.2]**. These experimental results and theoretical calculations using an envelope function scheme in the effective-mass approximation and on empirical tight-binding model seem to show type-I direct transitions in zincblende InAs/InP QWs **[3.3]**, although some calculations also predict type-II behavior **[3.4]**. In contrast, the electronic structure and optical properties of wurtzite InP and InAs are almost unknown.

The type-II behavior of wurtzite InP/InAs/InP CMS-NW is observed experimentally. Band-offset calculations based on the ”model-solid theory” of Van de Walle **[3.5]** for the wurtzite InP/InAs/InP heterostructure assuming three-dimensional compressive strain supports type-II band line-up.

3.2 Background

To start with, we provide the difference between type-I QW and type-II QW. **Figure 3.1 (a) and (b)** shows the schematic band line-ups of type-I QW and type-II QW, respectively. In the type-I QW system, both the electrons and the holes are confined at

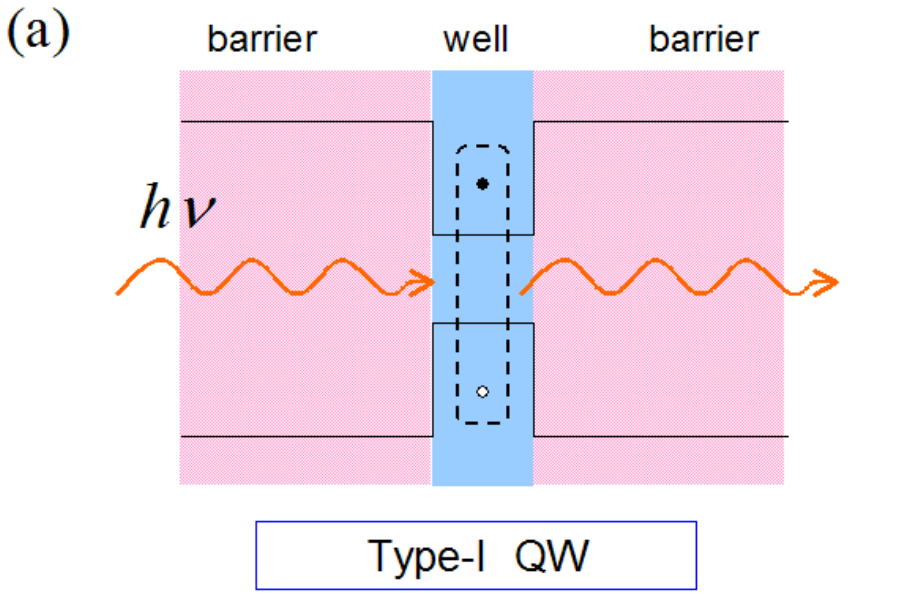

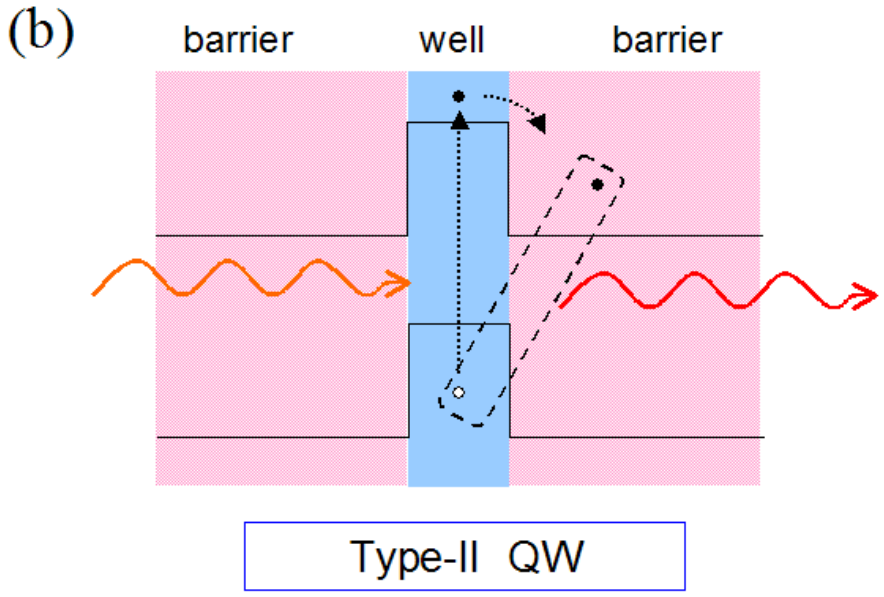

Figure 3.1 Schematic images of the type-I band line-up (a) and type-II band line-up (b).

the same well layer. Therefore the large overlapping the electron-hole wavefunction enhances the carrier recombination. On the other hand, in the type-II QW system, the electrons and the holes are confined in different layers. The overlapping electron-hole wavefunction is reduced, because the carriers are confined spatially separated. As a result, reduced career recombination causes the longer PL decay time. Moreover, type-II QW shows a large Stokes shift between absorption and luminescence because the absorption layer is located higher in energy than the luminescence layer.

3.3 Photoluminescence measurement

Figure 3.2 shows the PL spectrum of the sample taken under the following experimental conditions: Temperature is 2 K, excitation energy is 1.6 eV, excitation power is 10 mW, and excitation spot size is 50 μm in diameter covering ~10^4 CMS-NWs. It consists of multiple peaks. One ML fluctuation of the layer thickness is

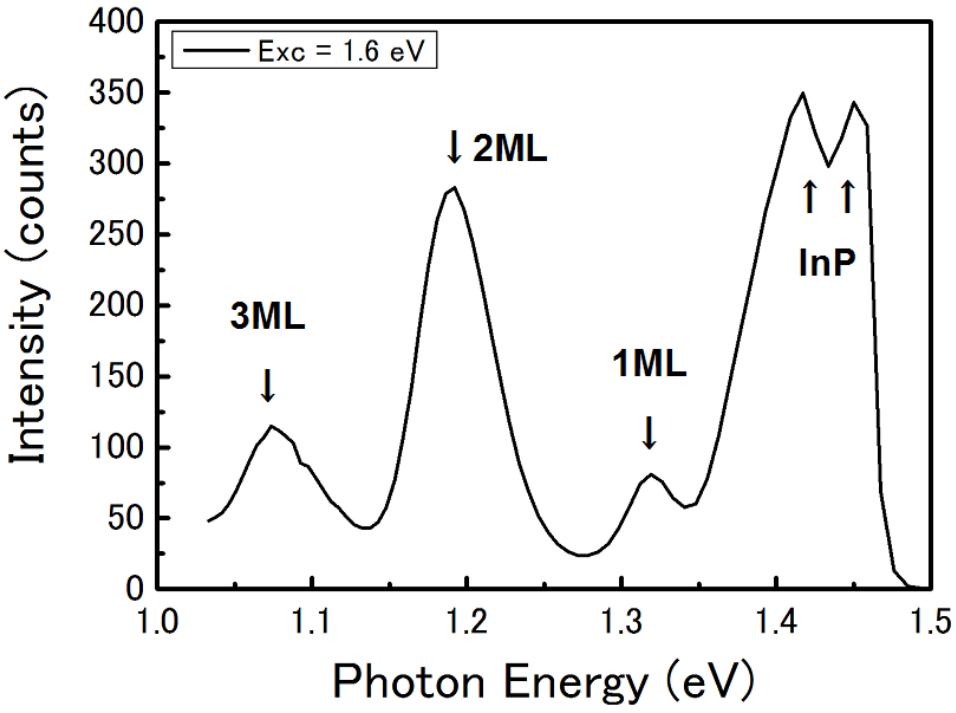

Figure 3.2 PL spectrum of InP/InAs/InP CMS-NW.

widely observed in the epitaxially grown semiconductor heterostructures. When the lateral dimension of the ML-islands is larger than the exciton in-plane diameter of the exciton, exciton recombination in ML-islands results in multiple peaks in the PL spectrum, as seen in **Figure 3.2**. Though the PL spectrum is obtained from the ensemble of CMS-NW, the multiple peaks are also observed is a single CMS-NW by means of micro-PL measurement (see **Figure 4.1**). Moreover, the PLE spectrum shows the exciton energy relaxation from 1-ML QW to 2-ML QW takes place, as described in section (3.5). Because the energy transfer from 1-ML QW to 2-ML QW takes place more probably in a single CMS-NW than between 2 CMS-NWs, one ML fluctuation is considered to be contained even in a single CMS-NW. Here, we assign the PL peak energies based on the calculation of the lowest-energy transition in a strained InAs/InP QW by using effective mass approximation. Peaks at 1.07, 1.18, and 1.32 eV in the spectrum correspond to transition energies in InAs QWs 0.60, 0.44, and 0.27 nm thick, respectively. Minimum width for InAs in InP is realized by substituting one layer of P for one layer of As. It corresponds to half monolayer thickness for (110). Thus, in the elastic continuum model, the thinnest InAs QW is expected to be 0.219 nm **[3.6]**, and the well width should be its multiple. This assignment is in approximate agreement with other experimental and theoretical results available in the literature on ultrathin InAs/InP QWs **[3.7]**. We label the PL band energies ranging from 1.32 eV to 1.07 eV to the regions of nominal thickness 1, 2, and 3 MLs, respectively. The 1.45 and 1.42 eV peaks are assigned to the wurtzite (wire) InP and the zincblende (substrate) InP, respectively.

3.4 Temperature dependence of photoluminescence

Next, we measured temperature dependence of PL to examine a non-radiative process. **Figure 3.3 (a)** shows the PL spectra at 6 different temperatures. Beyond 50 K, PL intensity decreases quickly. When temperature becomes higher than 120 K, the spectral tail of InP appears at the higher energy side coming from the red shift of the band edge of InP. We make an Arrhenius plot of the PL peak intensity as shown in **Figure 3.3 (b)**: Plot of logarithm of the PL peak intensity against the inverse of temperature. The fitting is done by an Arrhenius equation with an activation energy of E_a = 5.9 meV,

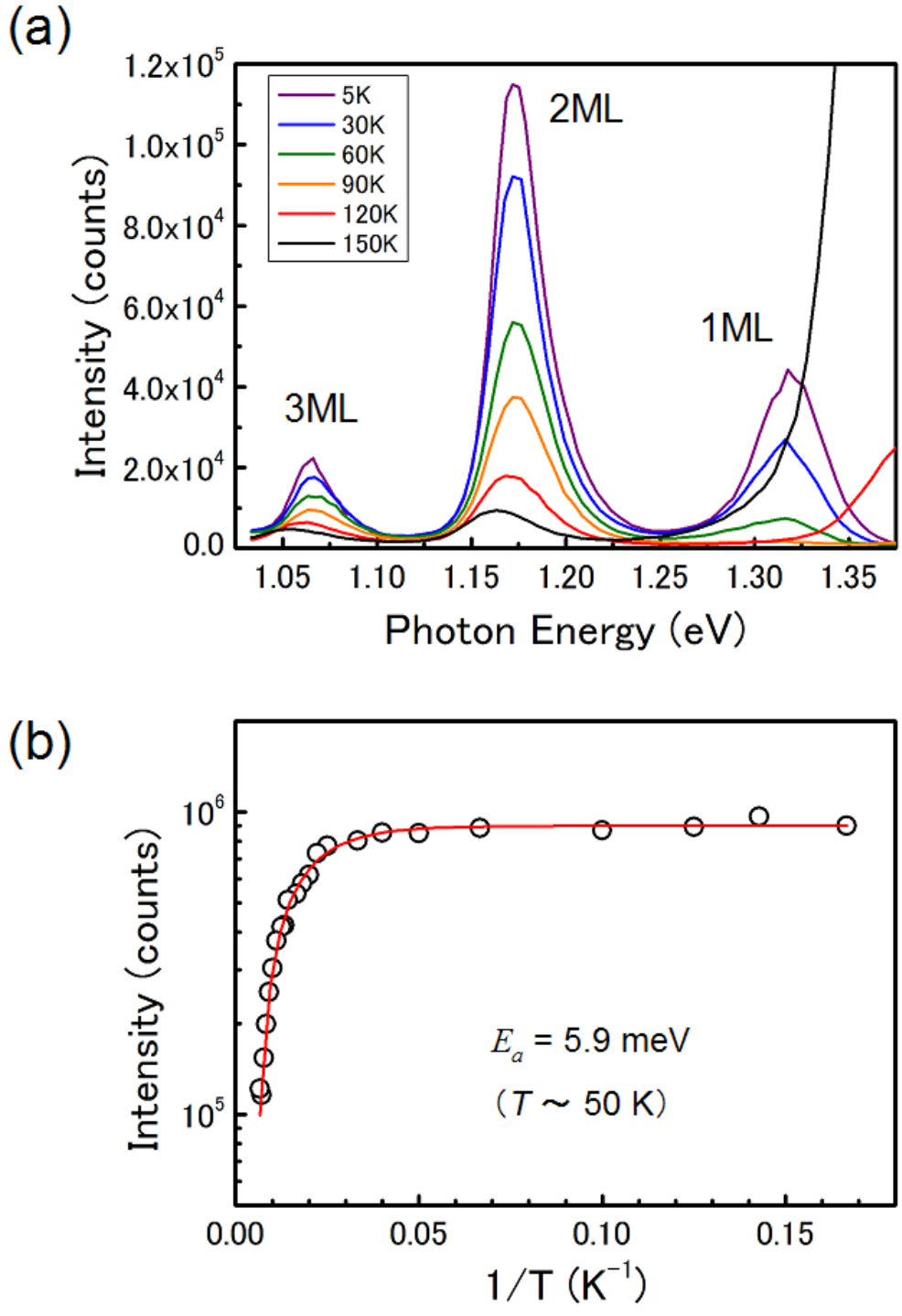

Figure 3.3 (a) Temperature dependence of PL spectra. (b) Arrhenius plot of PL peak intensity and its fitting curve.

$$I = A \cdot e^{-\frac{E_a}{k_B T}} \quad . \qquad (4.1)$$

The temperature corresponding to the activation energy is 50 K. This suggests that non-radiative processes become effective above 50 K. Therefore, we must reduce the temperature less than 50 K to observe only the radiative process.

3.5 Photoluminescence excitation measurement

Now, we measure PL excitation (PLE) spectra. **Figure 3.4** shows the PLE spectra for detection at 1-ML (open circle) and 2-ML (filled circle) PL peaks. Rise of the PLE signal at about 1.5 eV is assigned to absorption of the wurtzite InP layer. The shoulder-like structures at 1.25 and 1.39 eV may be assigned to the absorption of 2-ML and 1-ML InAs QW regions, respectively. We note that the PLE spectrum measured at the 2-ML PL peak shows a structure at 1.39 eV, where the absorption of the 1-ML peak appears. This indicates that carrier relaxation from the 1-ML QW region to 2-ML QW regions (lateral migration) takes place within a CMS-NW, possibly through the interaction with phonons. We observe a large Stokes shift of 70 meV between PL and PLE spectra. The full width at the half maximum (FWHM) of PL peaks is 30 meV. Broad PL peaks may be caused by the inhomogeneous broadening arising from short-range monolayer fluctuations and intermixing of As and P at the interface. However, the Stokes shift is too large to be explained by the inhomogeneous broadening only. It is known that the Stokes shift for the inhomogeneously broadened exciton PL band almost universally becomes 0.6 times of the FWHM of the excitonic absorption band for QWs. This universality is based on a large number of experimental observations and is also supported by theoretical calculations **[3.8]**. In our case the Stokes shift (70 meV) is more than twice the PL linewidth of 30 meV. Relaxation in an inhomogeneously broadened band can not explain such a large Stokes shift. The large Stokes shift possibly arises from type-II transition **[3.9]**, because the absorption takes place at a higher energy than the PL in the type-II system.

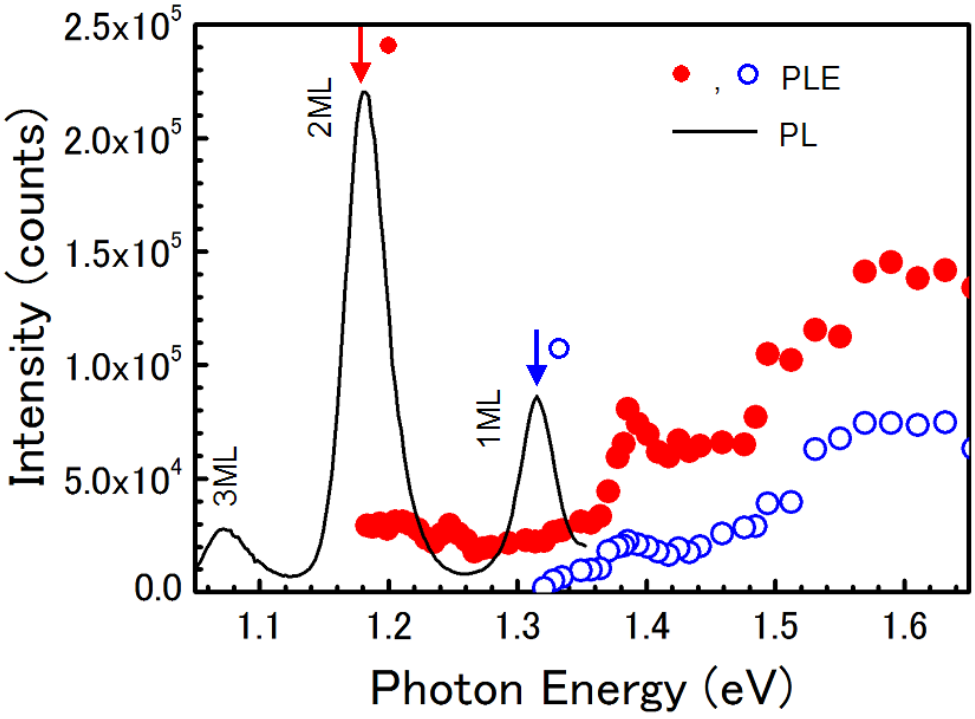

Figure 3.4 PL (solid line) and PLE spectra for detection at 1 ML (open circle) and 2 ML (filled circle) PL peaks.

3.6 Temporal change of PL peak

For type-II transitions, PL decay time is known to be long (several tens of nanoseconds) due to reduced overlap of the electron-hole wave functions **[3.10]**. Decay of PL signal at the 2-ML peak is recorded by means of standard TCSPC **[3.11].** It is shown in the semilogarithmic plot in **Figure 3.5**. We observe a slow and nonexponential decay. Identical behavior is observed in other peaks. This indicates type-II transition, because long decay time in **Figure 3.5** can not come from type-I transitions. Recently Tomimoto *et al*. studied zincblende 2 ML type-I InAs/InP QWs that show a PL decay time of 1–2 ns **[3.12]**. We note that nonradiative recombination is negligible in our sample at low temperatures, because the integrated PL intensity and PL decay rate are nearly independent of temperature up to 50 K. We attribute the nonexponential decay of PL in **Figure 3.5** to a distribution of decay rates arising from inhomogeneities at the

interface due to monolayer fluctuations and intermixing of As and P. Nonexponential decay resulting from a distribution of decay rates is often fitted by the function **[3.13,3.14]**

$$I_{PL} \propto \frac{I_0}{(1+2\Gamma t)^{\beta}} \quad , \qquad (3.2)$$

if nonradiative decay can be neglected, as it is in our case. Here, I_0 is the PL intensity at t = 0, Γ is an effective decay rate, and the exponent β depends on decay mechanism, distribution of decay rates, etc. We fit the TR-PL data in **Figure 3.5** using the above function. Best fit to our data yields $\beta = 2.5 \pm 0.02$ and $\Gamma = 0.06 \pm 0.006$ ns^{-1}, giving an effective PL decay time of about 16 ns. Such a long decay time reflects the feature of the type-II system.

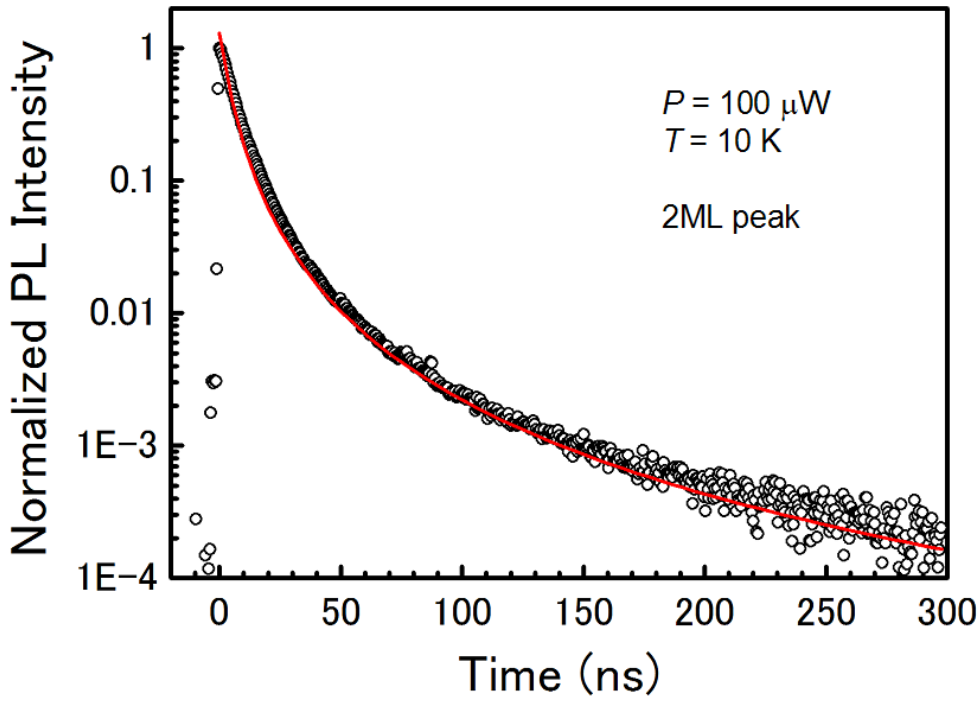

Figure 3.5 Temporal change of PL signal at the 2 ML peak (a open circle) and its fitting curve (a solid line).

3.7 Model-solid theory

Calculation of electronic energy levels for wurtzite InP/InAs/InP CMS-NWs having the three-dimensional strain distribution, the cross section in hexagonal symmetry and the translational symmetry along the NW axis is a complex task and is not available in the literature. For simplicity, we take the following approaches to calculate the conduction and valance band offsets based on the model-solid theory of Van de Walle **[3.5]**. Here, InAs and InP have a wurtzite crystal structure in our sample, and a thin InAs shell is completely buried between thick InP layers (**Figure 2.2**), which will force the InAs lattice constant in the radial direction to be that of InP. Also the epitaxial growth of the sample makes the InAs lattice constant in the axial direction the same as that of InP. We may assume that the InAs layer is under hydrostatic pressure, which results in compressive strains in all three directions. We take the *c*-axis lattice constant of wurtzite InAs **[3.6]** (InP **[3.15]**) to be c = 6.9 (6.6) Å and use c/a = 1.633 (a is the lattice constant in the plane perpendicular to the *c*-axis) **[3.16]**. Then using the formalism and parameters from **Ref. 3.5**, we obtain the type-II band alignment with the conduction (valance) band of InAs lying 0.16 (0.32) eV above the conduction (valance) band of InP. Details of the band line-up calculation by using model-solid theory are described in next paragraph.

The theory is based on volume change of the well layer. The volume change comes form compressive (tensile) strain caused by lattice missmatch between the well layer and the barrier layer. The strain tensor is written by

$$\varepsilon_i = \frac{a_{i,barrier}}{a_{i,well}} - 1 \quad , \tag{3.3}$$

where i denotes the crystal-axis. Here, we choose a coordinate with z axis parallel to the c-axis, and x and y axes parallel to the a-axis for the wurtzite crystal. Then the components of the strain tensor are simplified to be $\varepsilon_{xx} = \varepsilon_{yy} = \varepsilon_a$, $\varepsilon_{zz} = \varepsilon_c$. All the off-diagonal components are zero. Therefore the volume change is given by

$$\frac{\Delta\Omega}{\Omega} = \varepsilon_{xx} + \varepsilon_{yy} + \varepsilon_{zz} \quad . \tag{3.4}$$

The *relative* shift of the conduction band with respect to the valence band is expressed as

$$\Delta E_{v,av} = a_v \frac{\Delta\Omega}{\Omega} \quad , \tag{3.5}$$

where a_v is the hydrostatic deformation potential for the valence band. Similarly, the relative shift of the conduction band is

$$\Delta E_c = a_c \frac{\Delta\Omega}{\Omega} \quad . \tag{3.6}$$

Therefore, the volume change causes the band energy shift of $E^0_{v,av}$ and E^0_c:

$$\begin{aligned} E_{v,av} &= E^0_{v,av} + \Delta E_{v,av} \\ E_c &= E^0_c + \Delta E_c \end{aligned} \quad . \tag{3.7}$$

Usually, spin-orbit splitting (Δ_0) is include into the valence band, which gives the energy of the topmost valence band:

$$E_v = E_{v,av} + \frac{\Delta_0}{3} \quad . \tag{3.8}$$

For the heterojunction of *A/B*, energy discontinuity in the valence (conduction) bands is simply

$$\delta E^B_{v(c)} = E^{B(A)}_{v(c)} - E^{A(B)}_{v(c)} \quad . \tag{3.9}$$

When the valence (conduction) band energy in *B* is higher (lower) than the valence (conduction) band energy in *A*, the sign of δE_v is positive. δE_v and δE_c describes the band offset of the heterojunction of *A/B*.

Now, let us demonstrate how to derive band offset for the wurtzite InP/InAs heterojunction. Parameters used are shown in **Table 3.1**. The strain tensors for the InAs layer are calculated by using equation (3.3): ε_a = -0.048 and ε_c = -0.044. This indicates

the three-dimensional compressive strain is applied to the InAs layer. Equation (3.4) gives the volume change of $\Delta\Omega/\Omega = -0.139$. Relative shift of conduction (valence) band is derived as $\Delta E_c = 0.705$ eV ($\Delta E_{v,av} = -0.139$ eV). By using equation (3.7) and (3.8), E_c and E_v of InP InAs are calculated as follows:

$$E_c^{\mathrm{InP}} = E_c^0(\mathrm{InP}) = -5.580 \quad \mathrm{eV}$$
$$E_v^{\mathrm{InP}} = E_{v,av}^0(\mathrm{InP}) + \frac{\Delta_0(\mathrm{InP})}{3} = -7.003 \quad \mathrm{eV}$$
$$E_c^{\mathrm{InAs}} = E_c^0(\mathrm{InAs}) + \Delta E_c(\mathrm{InAs}) = -5.426 \quad \mathrm{eV}$$
$$E_v^{\mathrm{InAs}} = E_{v,av}^0(\mathrm{InAs}) + \Delta E_{v,av}^0(\mathrm{InAs}) + \frac{\Delta_0(\mathrm{InAs})}{3} = -6.682 \quad \mathrm{eV}$$

The band offset of valence (conduction) band is derived by equation (3.9):

$$\delta E_v^{\mathrm{InAs}} = E_v^{\mathrm{InAs}} - E_v^{\mathrm{InP}} = 0.32 \quad \mathrm{eV}$$
$$\delta E_c^{\mathrm{InAs}} = E_c^{\mathrm{InP}} - E_c^{\mathrm{InAs}} = -0.15 \quad \mathrm{eV}$$

The conduction band energy in InAs is higher than the conduction band energy in InP by 0.15 eV. This is the type-II band line-up.

Table 3.1 Parameters of wurtzite InP and InAs used for the model-solid theory calculation.

	a (Å)	c (Å)	a_v (eV)	a_c (eV)	$E^0_{v,av}$ (eV)	Δ_0 (eV)	E^0_c (eV)
InP	4.0 *	6.6 [a]	1.27 [c]	-5.04 [c]	-7.04 [c]	0.11 [c]	-5.58 [c]
InAs	4.2 *	6.9 [b]	1.00 [c]	-5.08 [c]	-6.67 [c]	0.38 [c]	-6.13 [c]

* $c/a = 1.633$ (Reference **[3.16]**)
[a] Reference **[3.15]**
[b] Reference **[3.6]**
[c] Reference **[3.5]**

3.8 Summary

Now, we summarize this chapter. We study optical properties of the periodic array of InP/InAs/InP CMNs by TR- and SR-PL and PLE measurements. A large Stokes shift more than twice the PL linewidth is observed between PL and PLE peaks. Moreover, slow and non-exponential decay of the PL peak with an effective decay time of 16 ns is observed in the TR-PL spectrum. Our study suggests the type-II optical transition. Band-offset calculation based on the model-solid theory supports the type-II band line-up arising due to the wurtzite crystal structure and triaxial (hydrostatic) compressive strain in these novel nanostructures.

References

[3.1]: R. Leonelli, C. A. Tran, J. L. Brebner, J. T. Graham, R. Tabti, R. A. Masut, and S. Charbonneau: Phys. Rev. B **48**, 11135 (1993).

[3.2]: P. Paki, R. Leonelli, L. Isnard, and R. A. Masut: Appl. Phys. Lett. **74**, 1445 (1999).

[3.3]: N. Shtinkov, P. Desjardins, and R. A. Masut: Phys. Rev. B **66**, 195303 (2002).

[3.4]: V. Albe and L. J. Lewis: Physica B **301**, 233 (2001).

[3.5]: C. G. Van de Walle: Phys. Rev. B **39**, 1871 (1989).

[3.6]: P. Mohan, J. Motohisa, and T. Fukui: Appl. Phys. Lett. **88**, 133105 (2006).

[3.7]: N. Shtinkov, P. Desjardins, and R. A. Masut: Phys. Rev. B **66**, 195303 (2002).

[3.8]: F. Yang, M. Wilkinson, E. J. Austin, and K. P. O'Donnell: Phys. Rev. Lett. **70**, 323 (1993).

[3.9]: T. T. Chen, C. H. Chen, W. Z. Cheng, W. S. Su, M. H. Ya, Y. F. Chen, P. W. Liu, and H. H. Lin: J. Appl. Phys. **93**, 9655 (2003).

[3.10]: C.-K. Sun, G. Wang, J. E. Bowers, B. Brar, H.-R. Blank, H. Kroemer, and M. H. Pilkuhn: Appl. Phys. Lett. **68**, 1543 (1996).

[3.11]: D. V. O'Conner and D. Phillips: *Time-Correlated Single Photon Counting* (Academic, New York, 1984).

[3.12]: S. Tomimoto, A. Kurokawa, Y. Sakuma, T. Usuki, and Y. Masumoto: Phys. Rev. B **76**, 205317 (2007).

[3.13]: M. V. Klein, M. D. Sturge, and E. Cohen: Phys. Rev. B **25**, 4331 (1982).

[3.14]: E. Finkman, M. D. Sturge, M.-H. Meynadier, R. E. Nahory, M. C. Tamargo, D. M. Hwang, and C. C. Chang: J. Lumin. **39**, 57 (1987).

[3.15]: P. Mohan, J. Motohisa, and T. Fukui: Nanotechnology **16**, 2903 (2005).

[3.16]: M. W. Larsson, J. B. Wagner, M. Wallin, P. Håkansson, L. E. Fröberg, L. Samuelson, and L. R. Wallenberg: Nanotechnology **18**, 015504 (2007).

Chapter 4.

Spectral diffusion

4.1 Introduction

We have studied basic optical properties of strain-induced InP/InAs/InP CMS-NWs and written that they show type-II behavior. In this chapter, we make PL spectroscopy and TR-PL spectroscopy of the sample to study the inhomogeneously broadened of the CMS-NW. Broad PL bands due to inhomogeneous broadening are observed by micro-PL measurement of even one CMS-NW. Transient dynamics of excitons in InP/InAs/InP CMS-NWs in the inhomogeneously broadened band is studied by means of a TCSPC technique. The spectral diffusion in both QW and QWR in the InP/InAs/InP CMS-NW is observed.

4.2 Micro-photoluminescence measurement

When the lateral dimension of the ML-islands is smaller than in-plane diameter of the exciton, ML fluctuation causes inhomogeneous broadening of the PL band and exciton localization. Broad PL peaks with FWHM of ~ 30 meV suggest inhomogeneous broadening (**Figure 3.2**). However, we can not determine what causes the inhomogeneous broadening so far. To know the origin of inhomogeneous broadening, we examine micro-PL measurement. Macroscopic PL collects PL of an ensemble of CMS-NWs because the PL is observed from a lot of ($\sim 10^4$) CMS-NWs, while micro-PL can observe PL of a single CMS-NW. The micro-PL measurement can answer to a question whether PL of a single CMS-NW has the inhomogeneous broadening or not. **Figure 4.1** shows the micro-PL spectra (solid lines) and the macroscopic PL spectrum (broken line). A remarkable thing is that the micro-PL spectrum has a broad PL bands similarly to the macroscopic PL spectrum. The important point of this result is that the broadening exists even in a single CMS-NW. We consider the inhomogeneous broadening originates from the well width fluctuation and the intermixing of As- and P-atoms at the heterointerface in a single CMS-NW **[4.1]**. These disorders at the heterointerface form potential fluctuation for excitons in a single CMS-NW.

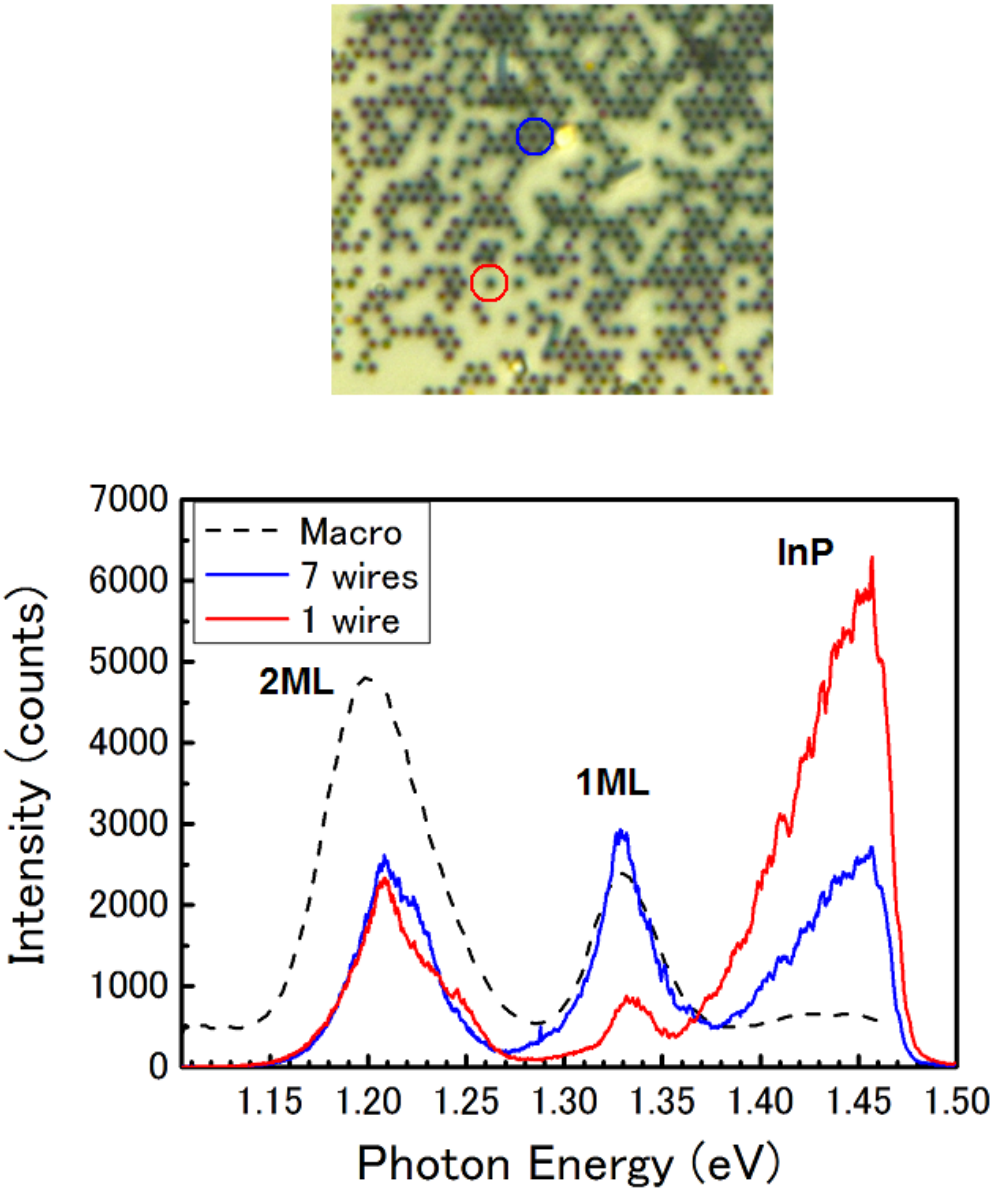

Figure 4.1 Micro-PL spectra (solid lines) and macroscopic PL spectrum (broken line).

4.3 One-dimensional and two-dimensional spectral diffusion

4.3.1 Time-resolved photoluminescence measurement

We made the TR-PL measurement around the 2ML PL band by using the TCSPC technique with the excitation energy density of I_0 = 7.5 mJ/m^2 per pulse. **Figure 4.2 (a)** shows a contour map of the energy- and time-resolved PL spectra. We plot in **Figure 4.2 (b)** the TR-PL spectrum at 1 ns and 10 ns, which clearly shows a spectral diffusion (time- dependent shift of the spectrum). The average energy of the 2ML PL band was calculated by using

$$\langle E(t) \rangle = \frac{\int E \cdot I_{PL}(E,t) dE}{\int I_{PL}(E,t) dE} . \qquad (4.1)$$

Here, we select the integration interval ranging from 1.125 to 1.225 eV: This corresponds to the interval ranging from the 1.125 eV valley to the 1.225 eV valley in a contour map shown in **Figure 4.2 (b)**. **Figure 4.3** shows a plot of the temporal change of the average energy. We can find a kink appearing at 1.3 ns and the two-stage spectral diffusion. We think that the kink comes from the transition from two-dimensional spectral diffusion to one-dimensional spectral diffusion in the CMS-NW. After the transition, the average energy decreases at the constant rate at least in the time ranging from 1.3 ns to 5.0 ns. The diffusion rate gradually slows down after 5.0 ns.

Let us pay attention to the first spectral diffusion observed within 1.3 ns time domain. It is found that the average energy of the 2ML PL band decreases at a constant rate (–1.98 × 10^6 eV/s) written by

$$\langle E(t) \rangle = -1.98 \cdot 10^6 \cdot t + 1.1775 \quad , \qquad (4.2)$$

where the average energy is written in the unit of “eV” and the time is in the unit of “s”. The spectral diffusion at a nearly constant energy-loss rate was reported in inhomogeneously broadened quantum well PL (the energy-loss rate ranging from −4.5 to −2.8 × 10^6 eV/s was observed in GaAs/AlAs multi-QW **[4.2]**). Therefore, we consider that the first spectral diffusion with constant energy-loss rate observed within 1.3 ns takes place in the QW region (side plane) of the CMS-NW. Similarly, the second spectral diffusion at a constant rate of -0.3 × 10^6 eV/s appears in the time ranging from

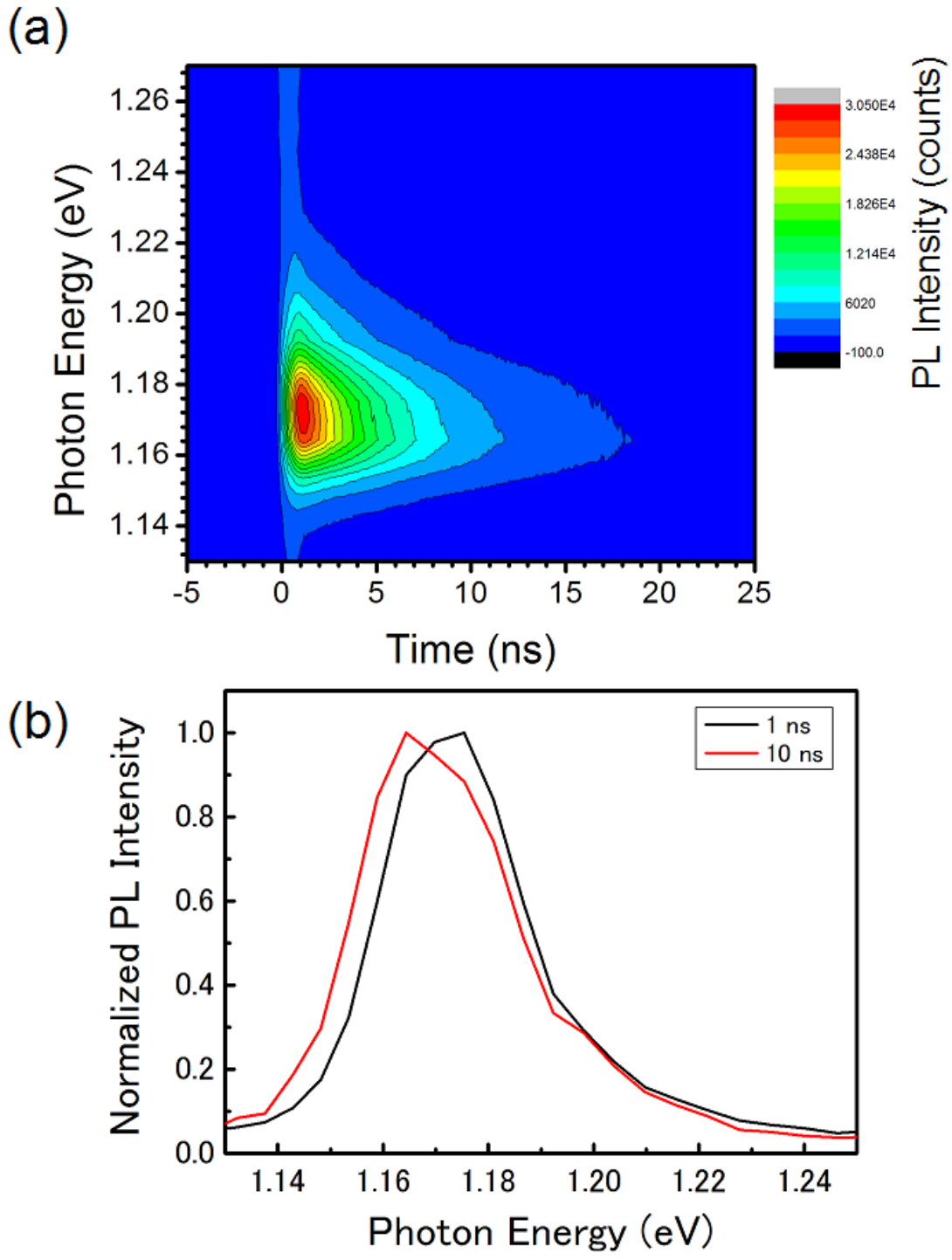

Figure 4.2 (a) A contour map of the TR-PL. (b) TR-PL spectra at 1 ns and 10 ns.

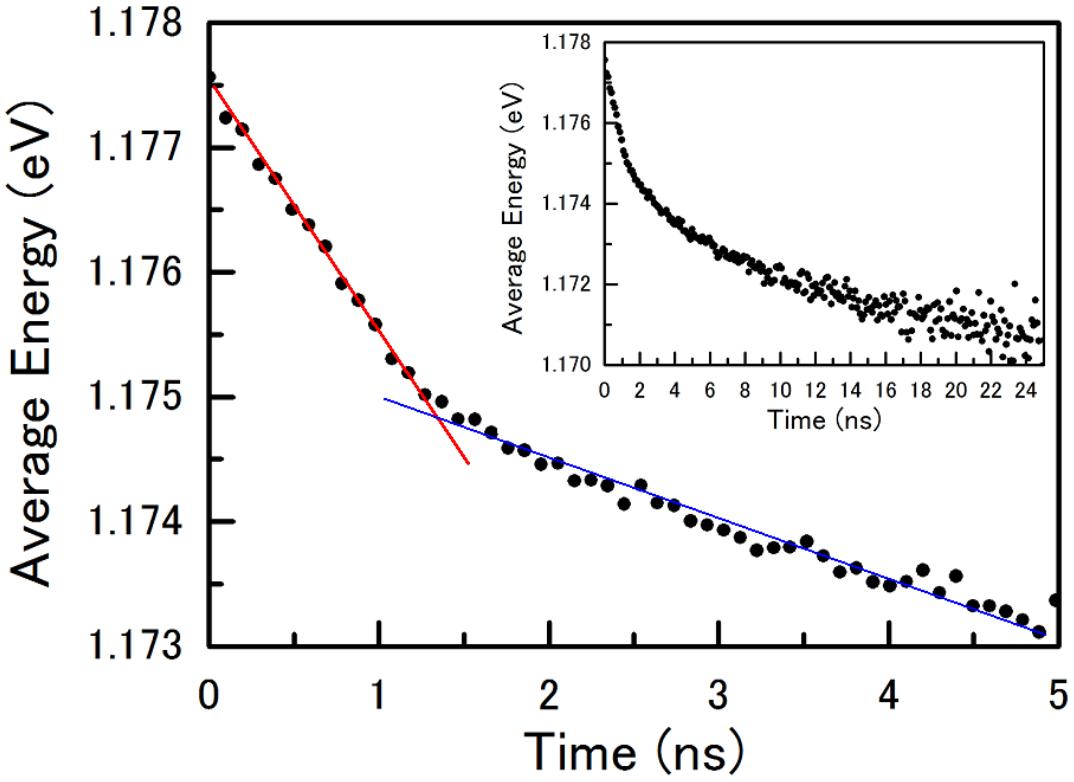

Figure 4.3 Temporal change of the average energy of the PL band in the time range of 0-5 ns. Inset shows in the temporal change of the average energy of the PL band the time range of 0-25 ns.

1.3 ns to 5.0 ns. We think that the second spectral diffusion takes place in at the QWR region (corner line) of the CMS-NW. The excitons confined in the side plane in the CMS-NW can move more easily in two-dimension than in one-dimension, leading to the first faster energy loss rate. On the other hand, the excitons in the corner line in the CMS-NW can move only in one-dimension. Therefore the excitons hardly find the lower energy position and they show the second slower diffusion.

4.3.2 Discussion

In the QW and QWR regions, an InAs layer is considered to consist of a number of clusters in which the layer width is constant and multiples of atomic layer thickness. Excitons are localized in respective clusters and the lateral size of each cluster is smaller than in-plane diameter of the exciton, because the absorption spectra of excitons do not show substructures (**Figure 3.4**). Excitons lose their energy slowly via the intercluster transfer process. **Figure 4.4** shows the distribution of the square clusters ξ long in *x* and *y* directions drawn by gray-scale pixels schematically. Localized excitons can only interact with phonons whose wavevectors are smaller than the inverse of the localization extent of excitons 1/ξ which is estimated to be in an order of $(10\ \text{nm})^{-1} = 10^6\ \text{cm}^{-1}$ **[4.2,4.3]**. As a result, only small-energy phonons (< 1 meV) participate

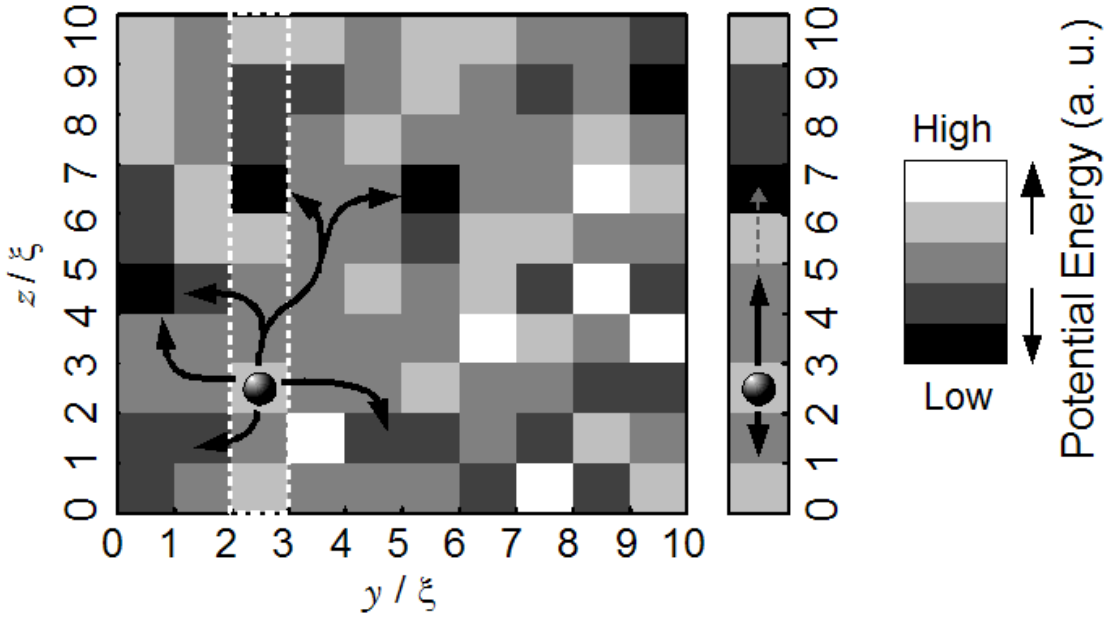

Figure 4.4 Cartoons for two- (left) and one-dimensional (right) exciton diffusions. Short-range potential fluctuations, drawn in gray-scale pixels, are given by random numbers that have a Gaussian distribution with a zero mean and a standard deviation of 1. Here ξ is the localization extent of excitons.

in the energy relaxation of localized excitons. This is the physical origin of the slow-energy relaxation. Therefore, we consider that the inhomogeneous broadening included in a single CMS-NW causes spectral diffusion at a constant and slow energy-loss rate. The small difference in energy loss rate between our result and that reported in Ref. **[4.2]** is based mainly on the differences in the substance, the type of QW, the exciton extent and the exciton-acoustic phonon interaction **[4.3]**. We consider that spectral diffusions in type-II band alignment undergo a minor change from those in type-I band alignment, because in the type-I exciton, both the electron and the hole are confined in the well layer, while in the type-II exciton, the electron and the hole are localized in different layers. Spectral diffusion for type-II excitons are different from type-I excitons, in the point that electrons and holes are localized in different layers. The deformation potentials of the valence (conduction) band of both the InAs and the InP are given as 1.00 eV (-5.08 eV) and 1.27 eV (-5.04 eV) respectivelly **[4.4]**. The difference in the deformation potentials of the valence (conduction) band between the InAs and InP is very small. In the case of the type-I exciton, both the electron and the hole are confined in the InAs well layer, and the difference in the deformation-potential between the conduction band and the valance band is -6.08 eV (= -5.08 – 1.00). On the contrary, in the case of the type-II exciton, where the hole is confined in the InAs well layer and the electron is localized in the InP barrier layer, the difference in the deformation-potential between the conduction band and the valance band is -6.04 eV (= -5.04 – 1.00). This is different from the deformation-potential for the type-I exciton by only 0.7 %. Therefore, the type-I exciton-deformation potential interaction is almost the same as the type-II exciton-acoustic phonon deformation potential interaction (Appendix. C).

In **Figure 4.3**, we can find that the energy-loss rate becomes slower after 1.3 ns. The slower energy-loss rate of -0.3×10^6 eV/s is about 7 times slower than the first energy-loss rate shown in the time region less than 1.3 ns (-1.98×10^6 eV/s). We consider that the difference between the two energy-loss rates depends on thet between the dimensions of the region where excitons are localized. The dimension-dependent energy-loss process of excitons is schematically shown in **Figure 4.4**. The excitons, confined in the QW region on the side plane in the CMS-NW, can move two-dimensionally. Therefore, these excitons can find the near and lower energy clusters more easily and migrate toward the lower energy positions in an inhomogeneous well. On the other hand, the excitons localized in the QWR region at the corner line in the CMS-NW move only one-dimensionally. This is because the energy in the corner region is lower than that in the side region by 2 meV, as is described below. Excitons hardly

find the nearby lower energy clusters in a wire. In the above-mentioned scenario, the spectral diffusion took place in two stages: the first (second) energy-loss rate indicates the two- (one-) dimensional spectral diffusion. To put it another way, the photo-excited excitons localized in the CMS-NW migrate from the side of the CMS-NW toward the corner of the CMS-NW.

We also show in **Figure 4.3** the two-dimensional spectral diffusion causes a 2 meV red-shift. This suggests that the exciton confinement energy in the QW region of the CMS-NW is higher than that in the QWR region of the CMS-NW by 2 meV. We calculate the energy levels and the hole wavefunction in both QW and QWR by using a finite element method (FEM). The one side of the hexagonal tube is selected for the FEM calculation, as shown in **Figure 4.5**. The barrier width is assumed to be 6 times thicker than the well width. The assumed barrier width is enough to converge the wavefunction. We lay the calculation range with triangular array of elements and

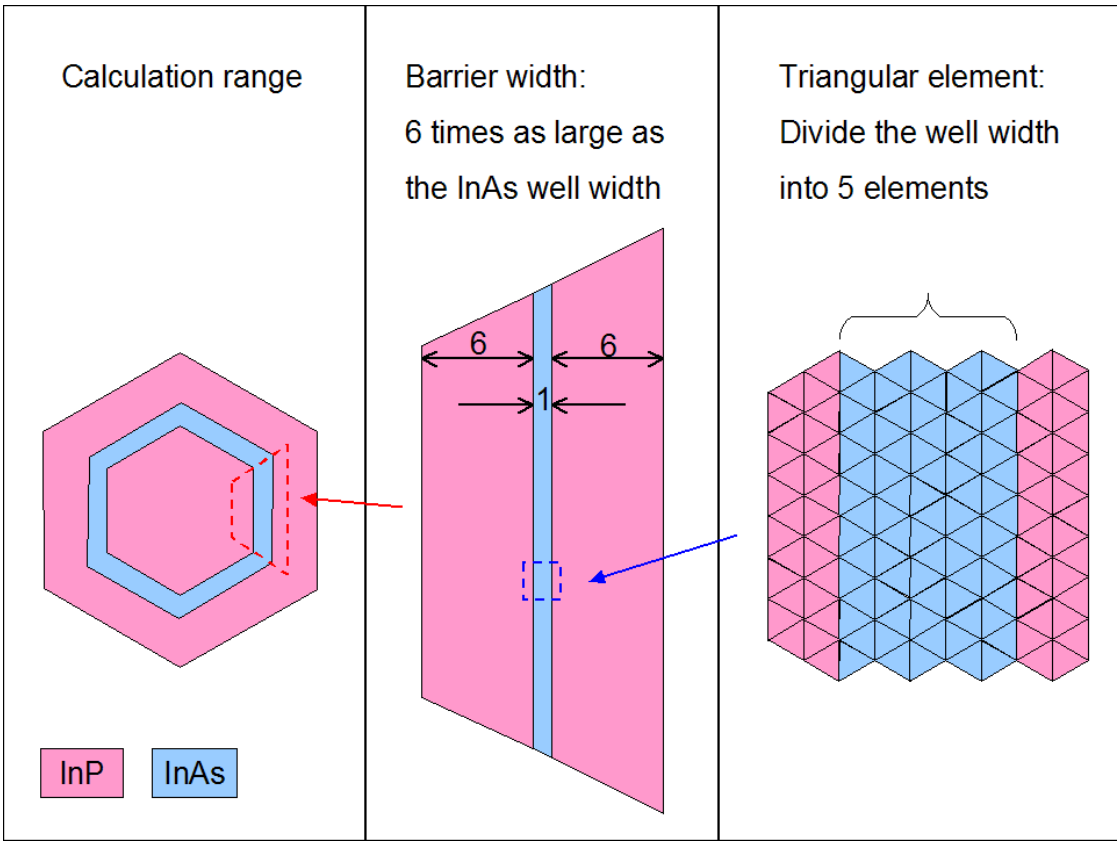

Figure 4.5 The schematic image of the FEM calculation range.

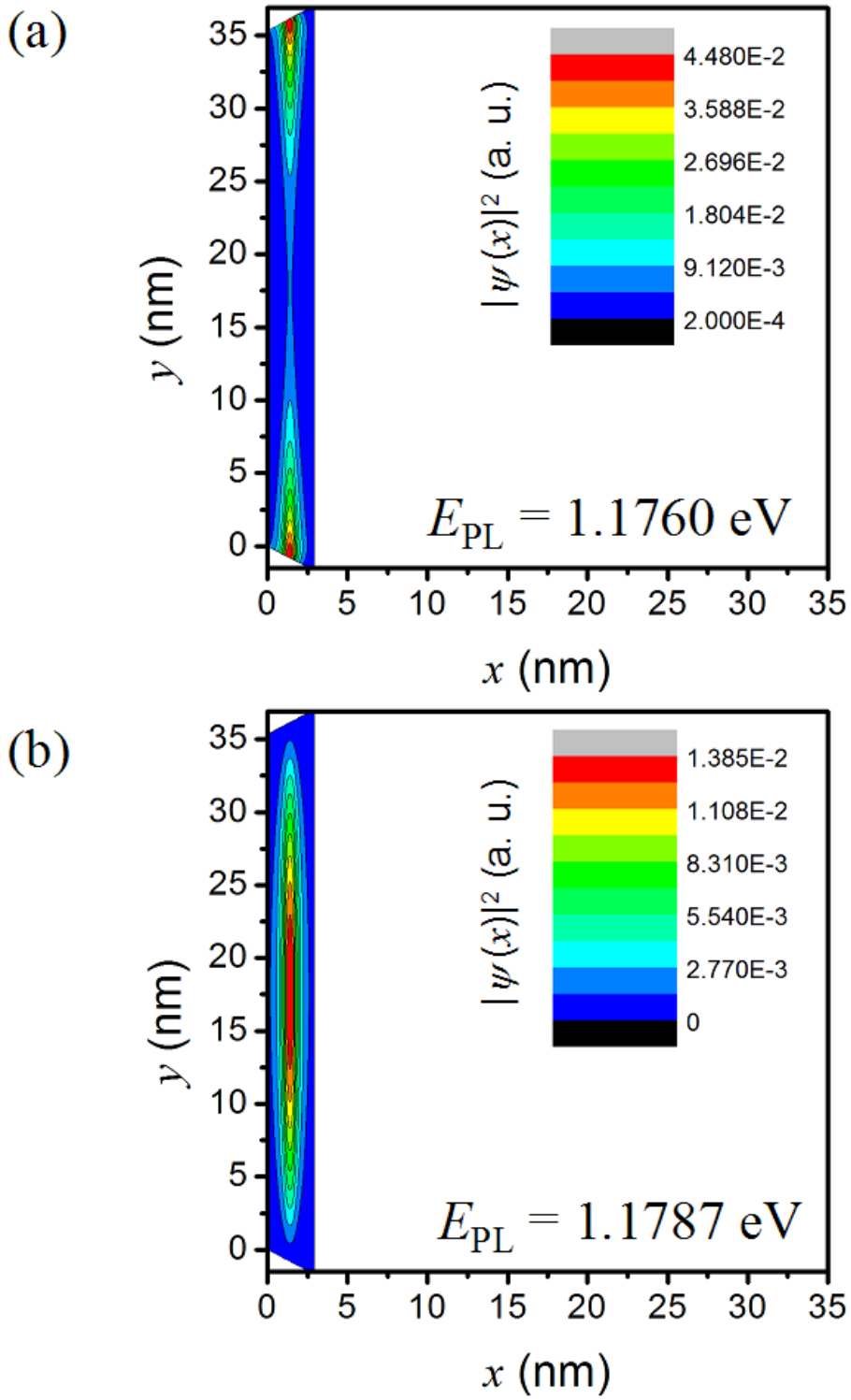

Figure 4.6 The contour maps of the hole wavefunction confined at the QWR region and QW region are shown in (a) and (b), respectively. The InAs layer region is shown in a broken line.

partition the well width into 5 elements. The contour maps of the hole wavefunction confined in the QWR region and QW region are shown in **Figure 4.6 (a)** and **(b)**, respectively. We find that the difference of the confinement energy between QW and QWR was 2.3 meV. This value exactly agrees with the energy shift from the beginning to the kink point. Accordingly, the excitons in the QW region move toward the QWR region showing the energy-loss of 2 meV.

4.4 Summary

Now, we conclude this section. The inhomogeneous broadening of a CMS-NW causes the spectral diffusion with a constant energy-loss rate. The spectral diffusion takes place in two stages. The first one is ascribed to spectral diffusion on the side plane in the CMS-NW and the second one is ascribed to spectral diffusion at the corner line in the CMS-NW. This suggests that photoexcited excitons in a core-multishell nanowire move from the two-dimensional side plane of the nanowire toward the one-dimensional corner line of the nanowire.

References

[4.1]: N. Shtinkov, P. Desjardins, and R. A. Masut: Phys. Rev. B **66**, 195303 (2002).

[4.2]: Y. Masumoto, S. Shionoya, and H. Okamoto: Proc. 17th Int. Conf. Physics of Semiconductor. (San Francisco, 1984) p. 349.

[4.3]: T. Takagahara: Phys. Rev. B. **31**, 6552 (1985).

[4.4]: C. G. Van de Walle: Phys. Rev. B. **39**, 1871 (1989).

Chapter 5.

Band bending

5.1 Introduction

Generally, the band bending effect in type-II quantum well system is explained on the triangular potential well model as follows. The spatially separated electrons and holes lead to the appearance of a strong electric field at the heterointerface which in turn gives rise to bending of the valence and conduction bands. With increasing excitation power, the band bending effect becomes more pronounced, and the accumulated electrons and holes will be confined in a narrower region near the interface. Consequently, the electron quantization energy increases and the blueshift occurs.

To analyze the amount of the blueshift, we should remember that photo-excited electron-hole pairs follow bimolecular recombination in our sample. The electron (hole) density n excited in the CMS-NW by the photon flux I is characterized by $n^2 \propto I$ (see Appendix A) **[5.1]**. The electrons are confined in a triangular potential well near the heterointerface formed by an electric-field strength of

$$F = \frac{en}{\varepsilon} \propto I^{1/2} \quad . \tag{5.1}$$

Here, ε is a permittivity of the barrier layer. The ground state of the electron confinement energy E_c in a triangular well is given by **[5.2]**

$$E_c = \left(\frac{\hbar^2}{2m}\right)^{1/3}\left(\frac{9\pi eF}{8}\right)^{2/3} \propto I^{1/3} \quad . \tag{5.2}$$

Thus E_c increases in proportion to the cube root of the excitation density. An important point to be considered further is the electrons and holes are spatially separated at the heterointerface in type-II band alignment. If the electron has extended far from the heterointerface, the electron confinement energy is not determined rightly in this triangular potential well model, because it is necessary to consider the electron

screening of Coulomb attraction by holes **[5.3]**. Therefore, we solve the Poisson equation and the Schrödinger equation self-consistently to determine an electron charge distribution, a potential shape and a confinement-energy.

5.2 Theory

The model calculation is explained as follows. In this model calculation, a potential shape and an electron wave function and a charge distribution are calculated self-consistently. A confinement-energy is calculated after the carrier density is given as an initial condition. The calculation routine is shown in **Figure 5.1**. Here, we regard the buried InAs layer as the one-dimensional quantum well confined by the InP barrier layers. The one-dimensional Poisson and Schrödinger equations are given by

$$\frac{d^2\phi(x)}{dz^2} = -\frac{1}{\varepsilon}\rho(x) \quad , \tag{5.3}$$

$$-\frac{\hbar^2}{2m}\cdot\frac{d^2\psi(x)}{dx^2} + \phi(x)\cdot\psi(x) = E_c\psi(x) \quad . \tag{5.4}$$

Here, ε and m are a permittivity and an effective electron mass of the barrier layer, respectively. The potential shape ($\phi(x)$) obtained from equation (5.3) is substituted into equation (5.4). The wave function ($\psi(x)$) obtained from equation (5.4) gives the charge distribution $\rho(x)$. We solve these two equation one after another by using a finite element method. Here, we approximate the initial potential shape as follows (schematic image are shown in **Figure 5.2**).

- The electron wave function penetrates almost through the potential barrier because the well width is very thin for the electron momentum. Therefore, we neglect the potential barrier for the electron.
- The most of the hole wave function exists in the InAs well layer because the hole effective mass is large. Therefore, we consider that the hole exists in the InAs well layer like the δ-function.

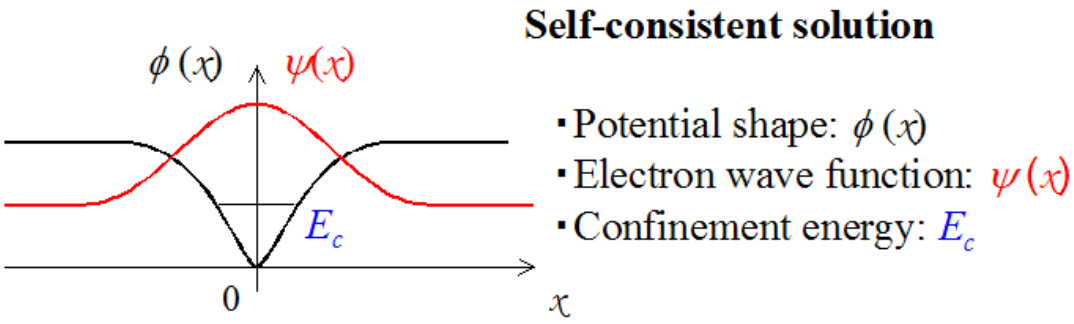

【calculation routine 】

Give a carrier density

↓

Electric field and charge distribution are calculated※

↓

Potential shape is calculated from Poisson equation※

↓

A wave function and a confinement energy in the calculated potential are solved by the finite element method.

↓

Electric field and charge distribution are calculated from a wave function

※ In the first calculation loop, the uniform electric field is adopted.
(triangular potential well approximation)

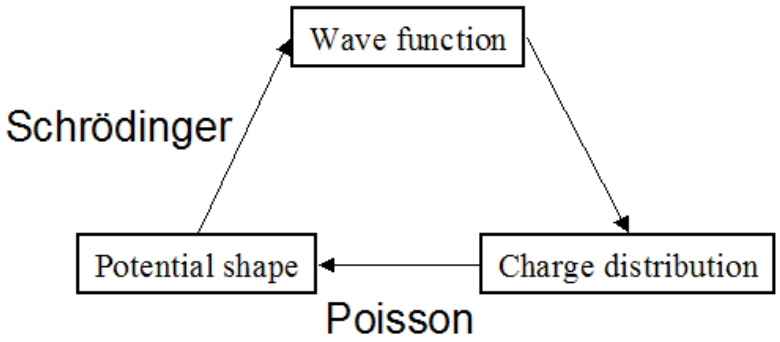

Figure 5.1 The routine of the model calculation.

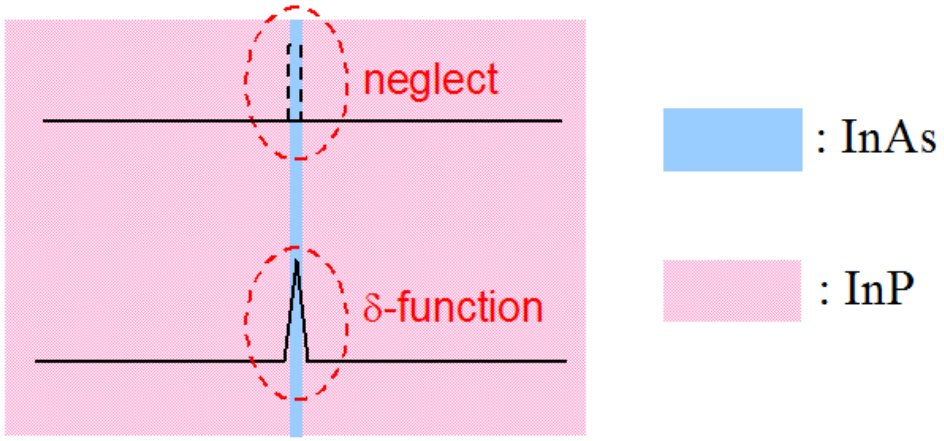

Figure 5.2 Approximation of the potential.

We calculate the electron wave function in two cases: the potential barrier height is finite or zero. Similarly, we calculate the hole wave function too. Calculation results are drawn in **Figure 5.3 (a)** and **(b)**, respectively. In **Figure 5.3 (a)**, the small difference is seen in the shape of the electron wave function in the heterointerfacial neighborhood. However, a good agreement is obtained as a "general extent" of the electron wave function because it penetrates almost through the potential barrier. Therefore, we can consider that the result of the Poisson equation changes little even if the potential barrier height is zero. On the other hand, the extent of the hole wave function is very small compared with that of the electron. We can consider that the hole wave function is in the well layer like the δ-function.

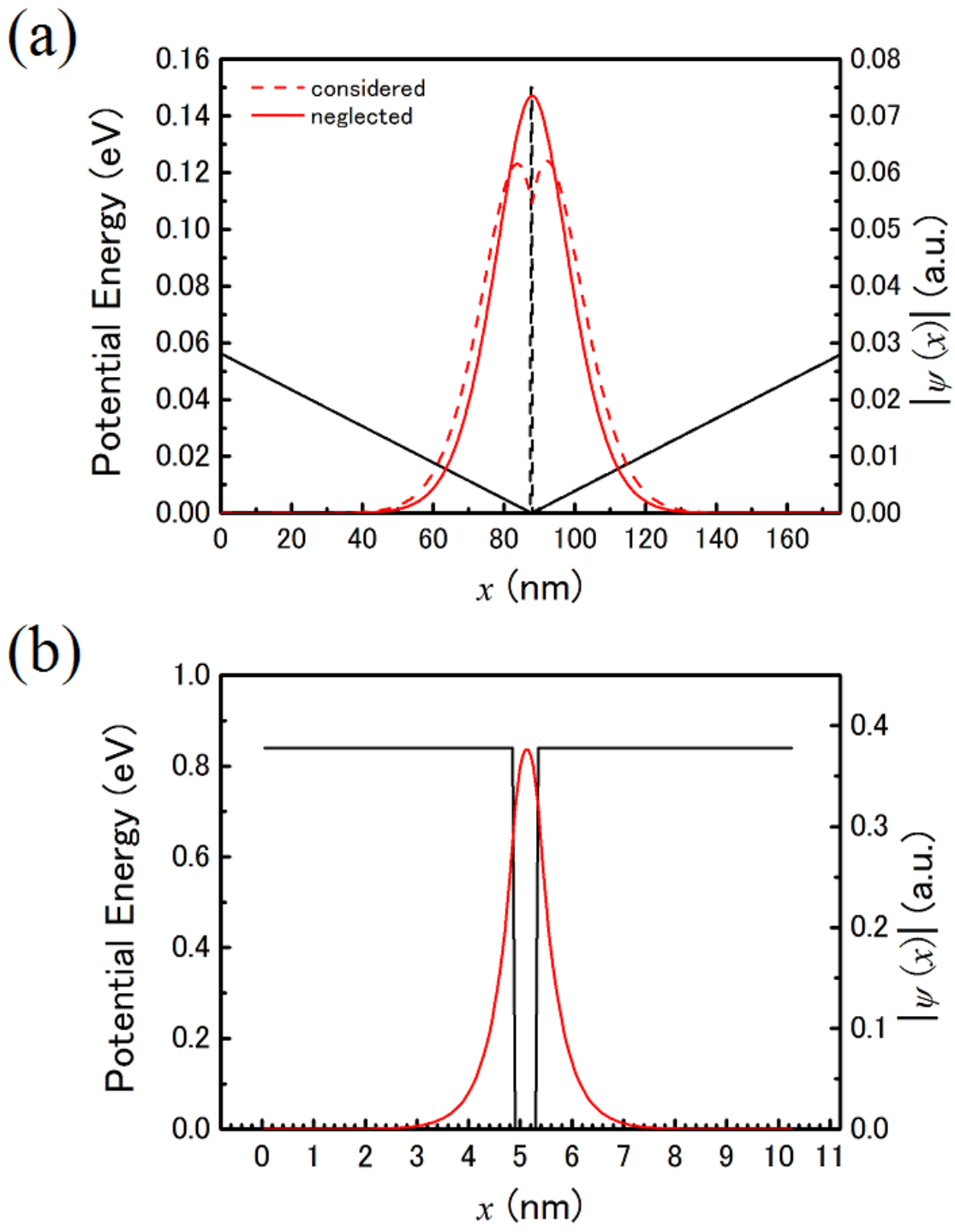

Figure 5.3 (a) The electron wave functions (a red line) and potentials (a black line) in the two cases: the potential barrier height is finite (a broken line) or zero (a solid line). (b) The hole wave function (a red line) and potential energy for the hole (a black line).

Next, we examine convergence of the calculation routine. The routine is shown in **Figure 5.1**. First of all, the carrier density evaluated from the excitation condition is given as an initial condition. The calculation loop is executed as follows.

1. The electric field formed by the Coulomb attraction of the hole and the screening by the spatial distribution of the electron are assume to be uniform. Therefore, the V-shaped potential is calculated. (This assumption is executed only in the first calculation loop.)
2. A wave function and a confinement-energy in the calculated potential are solved by using the Schrödinger equation (equation (5.4)) and the one-dimensional finite element method.
3. The charge distribution is given from a wave function solved above.
4. The potential energy is calculated from the charge distribution and the Poisson equation (equation (5.3)).
5. Return to the step 2.

This routine is repeated until the wave function, the restraint energy, and the potential shape are converged. **Figure 5.4** shows the numerical result at the carrier density of 12.75×10^{14} m^{-2}. Then the calculation routine is repeated about 15 times. It is found that potential, a wave function, and a confinement-energy converge. Moreover, it has been understood that the confinement energy becomes 8.22 meV. This value is lower than the result simply derived from the equation (5.2) (E_c = 26.4 meV). Thus, the triangular potential approximation is considered to give over-estimation of the confinement energy for the electron . The wave function has extended far from the heterointerface.

The relation between the electron density and the confinement energy was calculated by changing the electron density. The numerical result is shown in **Figure 5.5** (filled circle). We find that the confinement energy increases in proportion to the 2/3-th power of the electron density. We should remember that photo-excited electron-hole pairs follow bimolecular recombination in our sample. The carrier density n excited in the CMS-NW by the photon flux I is characterized by $n^2 \propto I$. This result reproduces the feature of the blue shift of the band bending, $E_c \propto I^{1/3}$. In addition, from **Figure 5.5**, we have found the relation between E_c (eV) and n (m^{-2}) described in the following equation (solid line).

$$E_c = 7.04 \cdot 10^{-13} \cdot n^{\frac{2}{3}} \quad . \qquad (5.5)$$

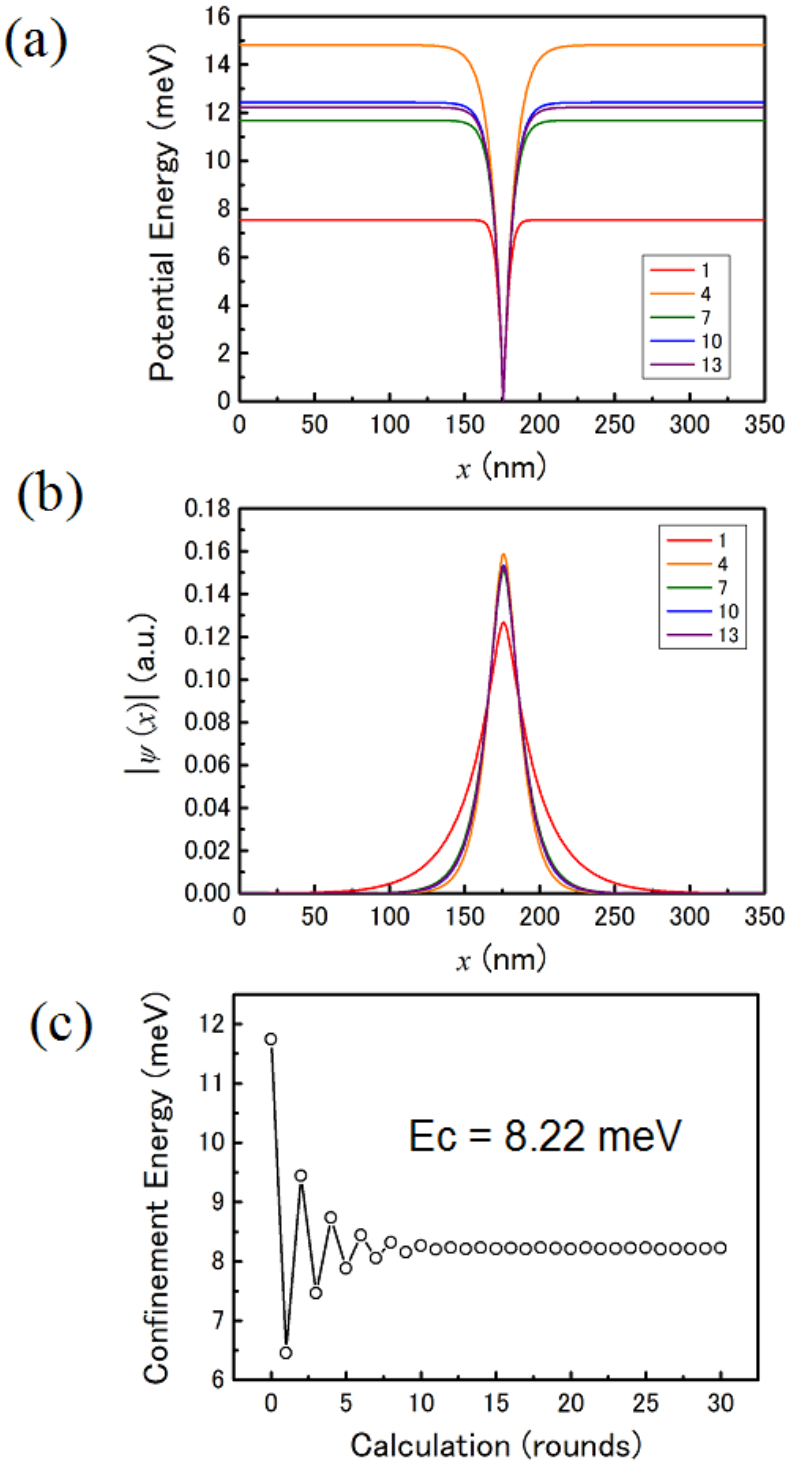

Figure 5.4 The numerical result of repetition of calculation routine, (a) potential energy for electron, (b) electron wave function, and (c) electron confinement energy, respectively.

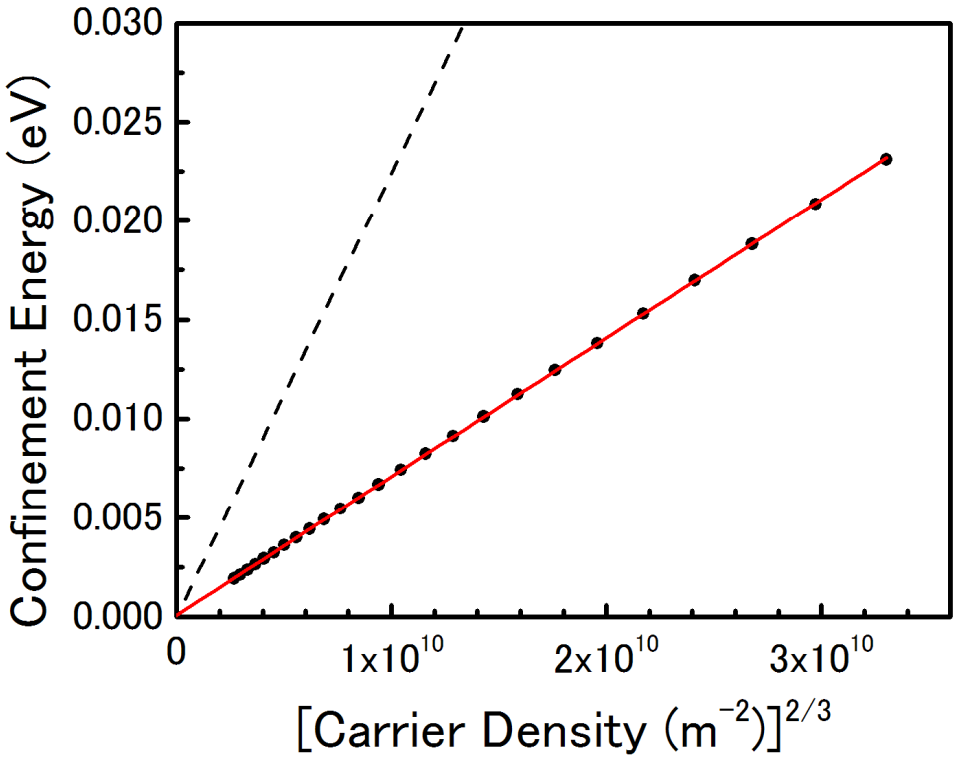

Figure 5.5 Comparison of the confinement energy of the model calculation (filled circle) with the triangular approximation (dashed line).

5.3 Excitation power dependence of photoluminescence

It has been shown in the literature by several authors **[5.4-5.6]** that a blue shift of the PL peak of a type-II optical transition is observed with the cube root dependence on the excitation power density P. In the type-II system the $P^{1/3}$ dependence of the transition energy arises from the band bending due to spatially separated electrons and holes. The theoretical background of the band bending is written in the section 5.2. PL spectra from our sample for 5 values of P are plotted in **Figure 5.6 (a)**. Blue shift of all the peaks with increasing P is evident. Peak energy position E_P as a function of $P^{1/3}$ for the each ML peak fits very well to a straight line in **Figure 5.6 (b)**. Identical behavior is observed in every peaks. Note that the blue shift of the PL peak is theoretically predicted to be linear with P due to state filling effect (Pauli exclusion principle) **[5.7]** and the linear blue shift was observed experimentally **[5.8]** in type-I QWs. We find in our experiments that the PL intensity increases linearly with P without any saturation in the range of P used. This shows that the recombination is excitonic in nature, and the excitation is in the low power regime where the state filling effect is negligible. Therefore, we consider that the $P^{1/3}$ dependence of the PL blue shift observed in **Figure 5.6 (b)** arises due to the type-II nature of our wurtzite InP/InAs/InP CMN sample.

Figure 5.7 (a) shows the excitation-power dependent 2 ML PL peak. The number of the excited electron-hole (*e-h*) pairs in a CMS-NW evaluated from the excitation power density is shown in the upper x-axis. The $P^{1/3}$ dependence of the PL blue shift is observed in the excitation power density ranging from $(4.0)^3$ to $(17.5)^3$ W/cm^2. The range is converted into the number of the *e-h* pairs in a CMS-NW ranging from 5 to 500. In other words, the band bending and the bimolecular recombination occur in this range. Above the excitation power density of more than $(17.5)^3$ W/cm^2, the blue shift is saturated, where the saturation of the absorption occurs. The absorption saturation is supported from the fact that saturation of the integrated PL intensity takes place beyond the same excitation power density of 5000 [~$(17.5)^3$] W/cm^2 (**Figure 5.7 (b)**). On the other hand, below the excitation power density less than $(4.0)^3$ W/cm^2, the $P^{1/3}$ dependence of the PL blue shift is not observed. We consider that the band bending and the electric field formed by the Coulomb attraction of the hole is negligible, when the number of *e-h* pairs generated in a CMS-NW is less than 5.

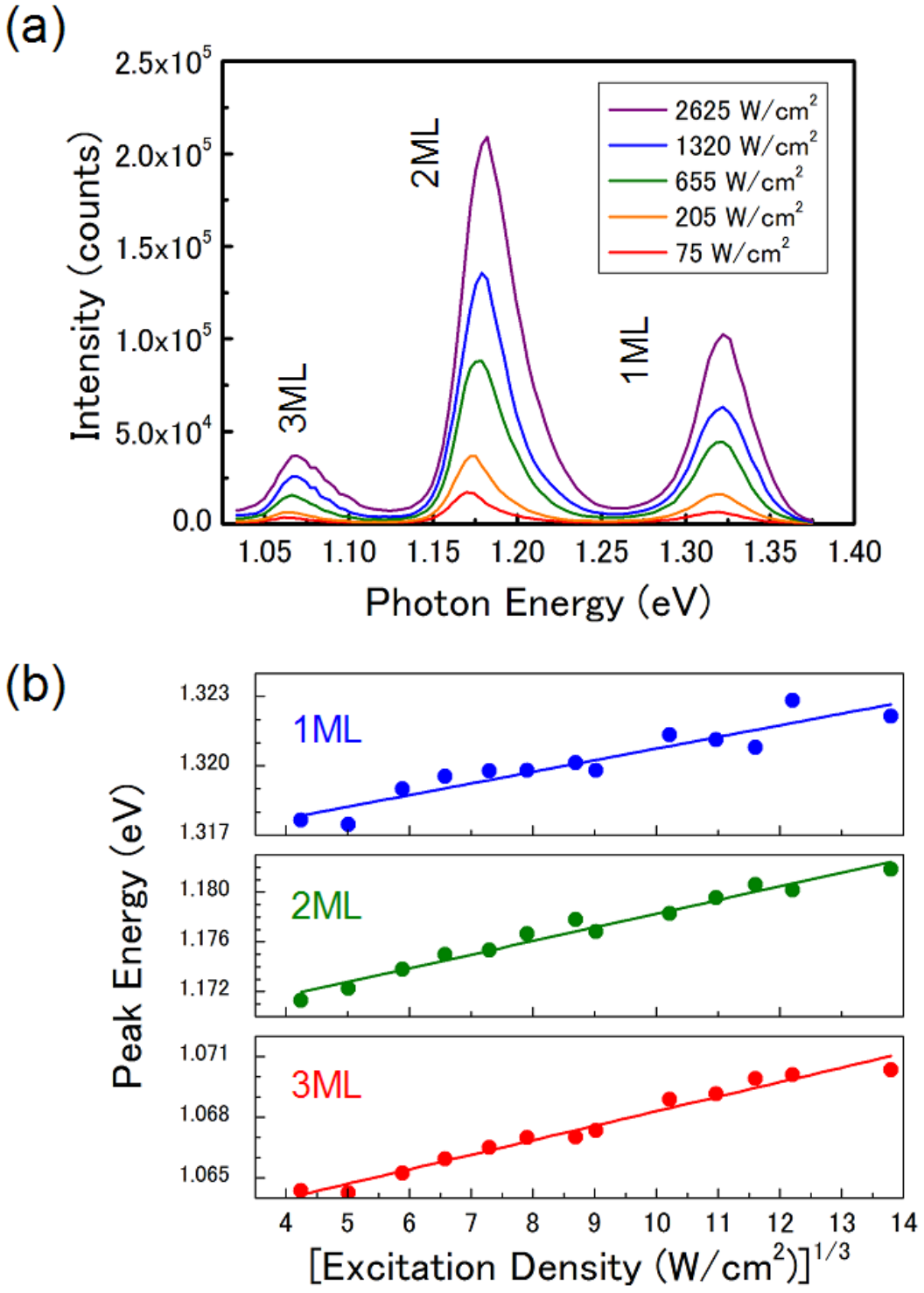

Figure 5.6 (a) PL spectra under 5 excitation densities. (b) PL peak energy position as a function of $P^{1/3}$.

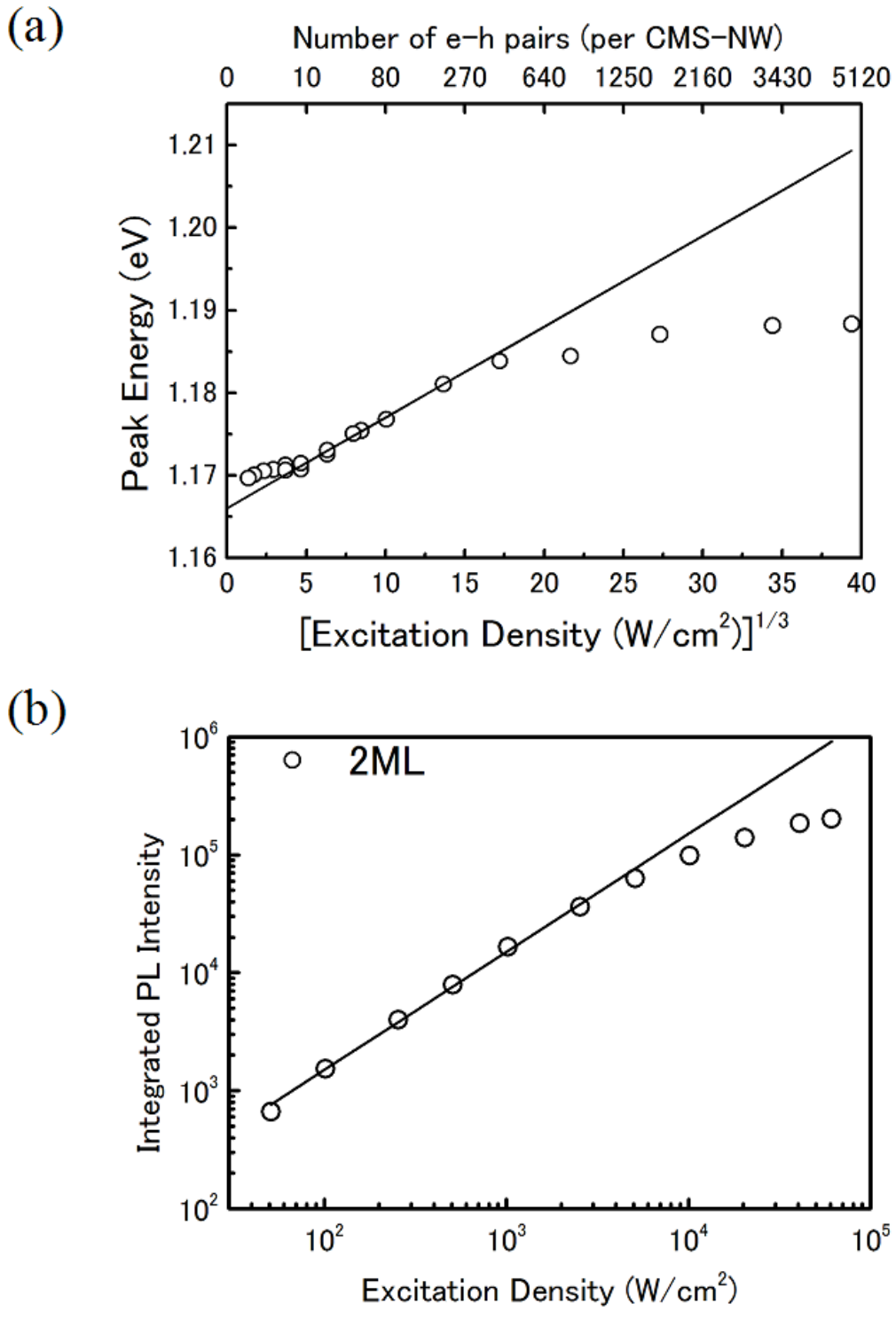

Figure 5.7 (a) 2ML PL peak energy position as a function of $P^{1/3}$. (b) Double logarithm plot of the integrated PL intensity versus the excitation power density with linear fit (solid line).

5.4 Transient band bending

5.4.1 Average energy of the photoluminescence band

Band bending is also observed in TR-PL. The PL decay is measured by means of a synchroscan infrared streak-camera. We measure the PL decay around the 2ML PL band. **Figure 5.8 (b)** shows temporal change of PL measured at the 2-ML peak (1.195 eV) and at the higher energy side of the band (1.23 eV and 1.275 eV) with the excitation energy density of I_0 = 1.2 J/m^2 per pulse. It generates 500 *e-h* pairs in the CMS-NW, and causes the band bending without any saturation. **Figure 5.8 (a)** is a contour map of the energy- and time-resolved PL spectrum. The fast decay is observed at the higher energy side of the PL band as indicated by a dashed circle. We consider that the fast decay is caused by the relaxation of the band bending. Moreover, we plot normalized PL spectra at 10 ps and 1000 ps, as shown in **Figure 5.9 (a)**. We can find clearly that the PL spectrum at 10 ps has higher energy component (hatching part). We identify that it comes from the transient band bending. Moreover, the PL peak shows red shift slightly as time proceeds. We think that this temporal red shift originates from the spectral diffusion.

Here, we calculate the temporal change of the average energy of the PL band for the discussion on the exciton dynamics by using equation (4.1). At this time, we select the integration interval ranging from 1.135 to 1.275 eV. This integration interval corresponds to the region ranging from the 1.135 eV valley to the 1.275 eV valley in a contour map. **Figure 5.9 (b)** shows a plot of the temporal change of the average energy. We should note that both the band bending and the spectral diffusion dynamics contribute to in the temporal change of the average energy. Therefore, it is necessary to subtract the effect of the spectral diffusion to see the band bending alone.

The spectral diffusion alone is seen in the time correlated single photon counting (TCSPC) measurement under the low excitation density by the following reasons.

- Under low excitation density, the density of the photo-excited excitons is very low and the band bending must be very small.
- In the Streak measurement, repetition period of the laser (12 ns) is shorter than photoluminescence lifetime. Therefore, the accumulating of the excitons takes place. On the other hand, the TCSPC measurement does not finds the effect of the accumulation of the excitons, because the repetition period of the laser (1.2 μs) is longer than the excitons recombination lifetime.

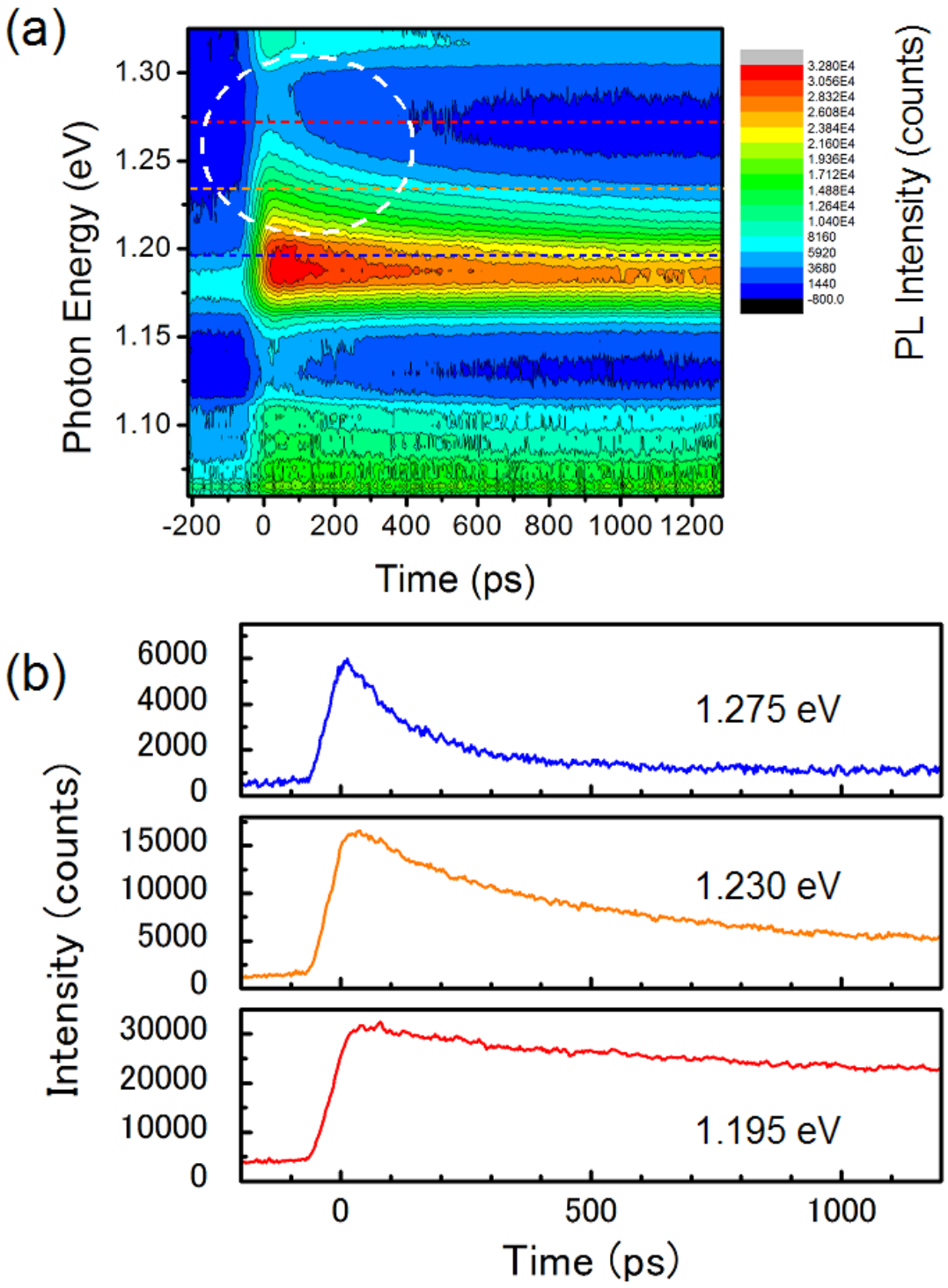

Figure 5.8 (a) A contour map of the TR-PL. (b) Temporal change of PL detected at the 2ML peak (1.195 eV) and at higher energy side of the band (1.230 eV, 1.275 eV).

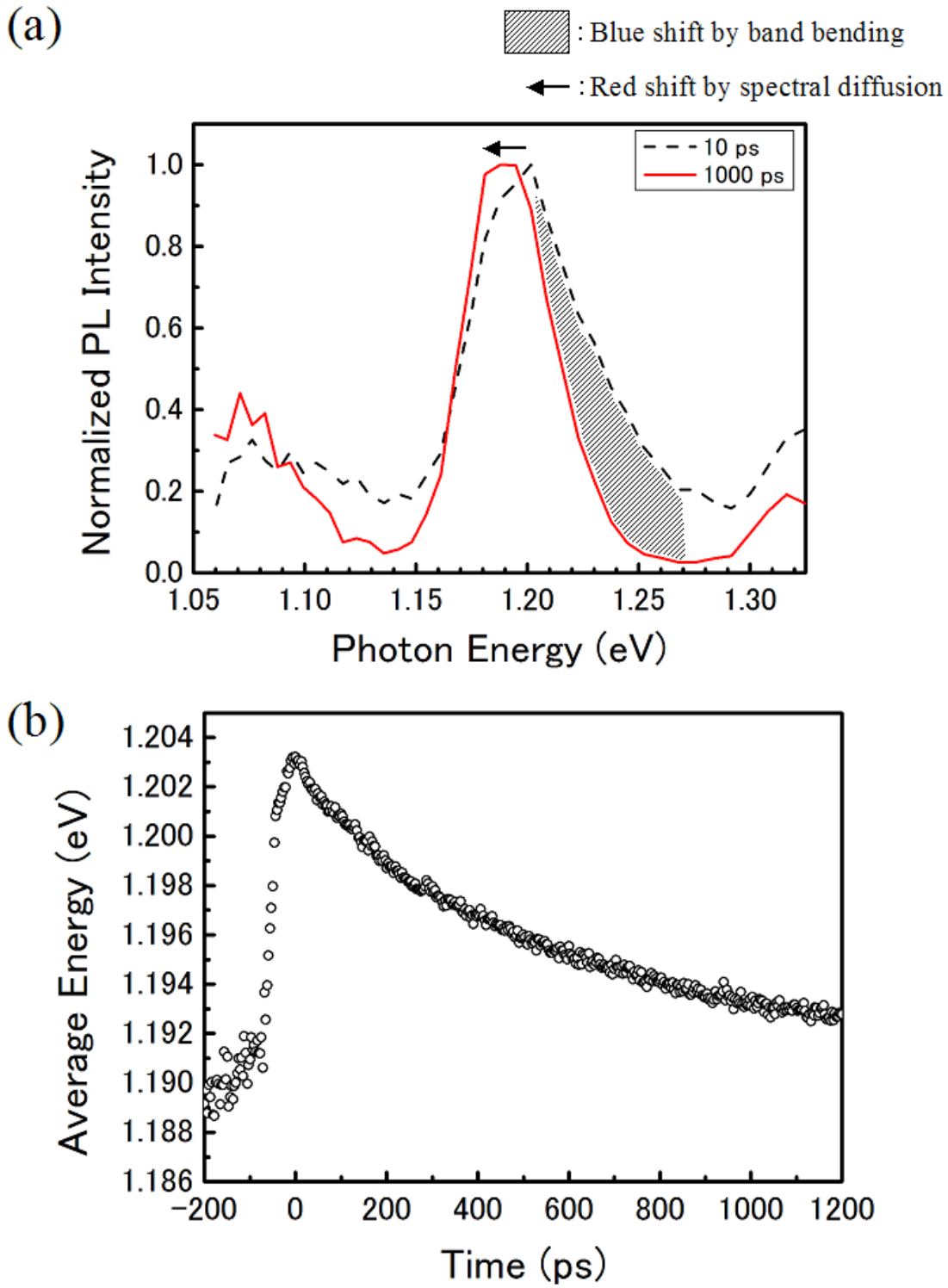

Figure 5.9 (a) TR-PL spectra at 10 ps and 1000 ps. (b) The temporal change of the average energy. It includes both the band bending and the spectral diffusion dynamics.

Therefore, we consider that the result of the TCSPC measurement under low excitation density shows the spectral diffusion alone: The influence of band bending is not included. In the previous chapter, **Figure 4.3** is measured under the excitation energy density of I_0 = 7.5 mJ/m^2 per pulse. It is weak enough to depress the band bending because it generates only 3.5 *e-h* pairs in a CMS-NW. On the other hand, we can consider that both the spectral diffusion and the transient band bending are observed in the result of Streak measurement under the excitation energy density of 1.2 J/m^2.

Now, let us subtract the effect of the spectral diffusion from the result of the streak camera measurement (**Figure 5.9 (b)**) by using the equation (4.2). **Figure 5.10 (a)** shows a result of the subtraction. The temporal change of the confinement energy obtained here is considered to be the change of the blue shift caused by the band bending. The confinement energy is shown to shift with increase of the electrion density due to the band bending as is written by equation (5.5). By using equation (5.5), the time-dependent confinement energy E_c is converted into the time-dependent exciton density n. The temporal change of the exciton density converted from that of confinement energy is shown in **Figure 5.10 (b)**.

Here, we pay attention the exciton density before and after the pulse excitation. Before the excitation, the excitons remain to be about 3.2×10^{15} m^{-2}. After the excitation, the excitons increased to 7.0×10^{15} m^{-2}. Therefore, 3.8×10^{15} m^{-2} excitons are generated by the pulse excitation. We estimate the exciton density of 3.4×10^{15} m^{-2} by considering the excitation energy density of I_0 = 1.2 J/m^2 per pulse (Appendix B). A good agreement is obtained. In the next step, we discuss the dynamics of the transient band bending by using this temporal change of the exciton density.

The integrated PL intensity S_{PL} is calculated by

$$S_{PL}(t) = \int I_{PL}(E,t)dE \quad . \tag{5.6}$$

At this time, we select the integration interval ranging from 1.135 to 1.275 eV: It is the same interval that is used to derive the average energy of the PL band. **Figure 5.11 (a)** shows the temporal change of the integrated PL intensity obtained from the energy- and time-resolved PL spectra shown in **Figure 5.8 (a)**. Now, let us think a decrease of the exciton density by radiative recombination process. In our sample, the excitons recombine by bimolecular recombination process. Therefore, we expect that S_{PL} decreases in proportion to n^2 ($I \propto n^2$). **Figure 5.11 (b)** shows the normalized temporal change of S_{PL}, $n(t)$, and $n^2(t)$. Here, good agreement between $n(t)$ and S_{PL} is found. This

indicates that the decrease of the exciton number, caused by bimolecular recombination, does not cause the decrease of the exciton density. Then, we consider what causes a decrease of the exciton density in the next section.

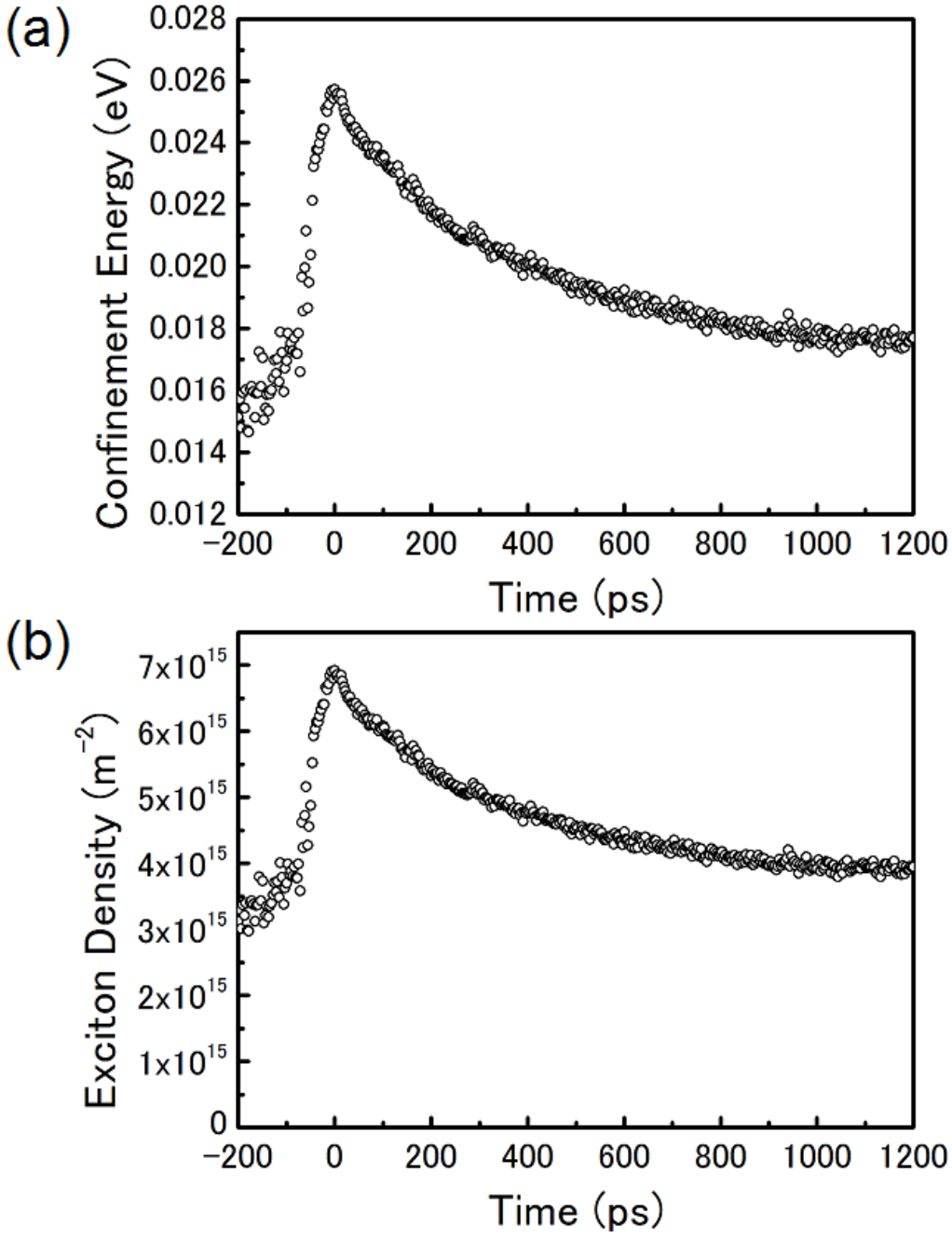

Figure 5.10 (a) The temporal change of the confinement energy. It comes from the relaxation of blue shift caused by the band bending. (b) The temporal change of the carrier density.

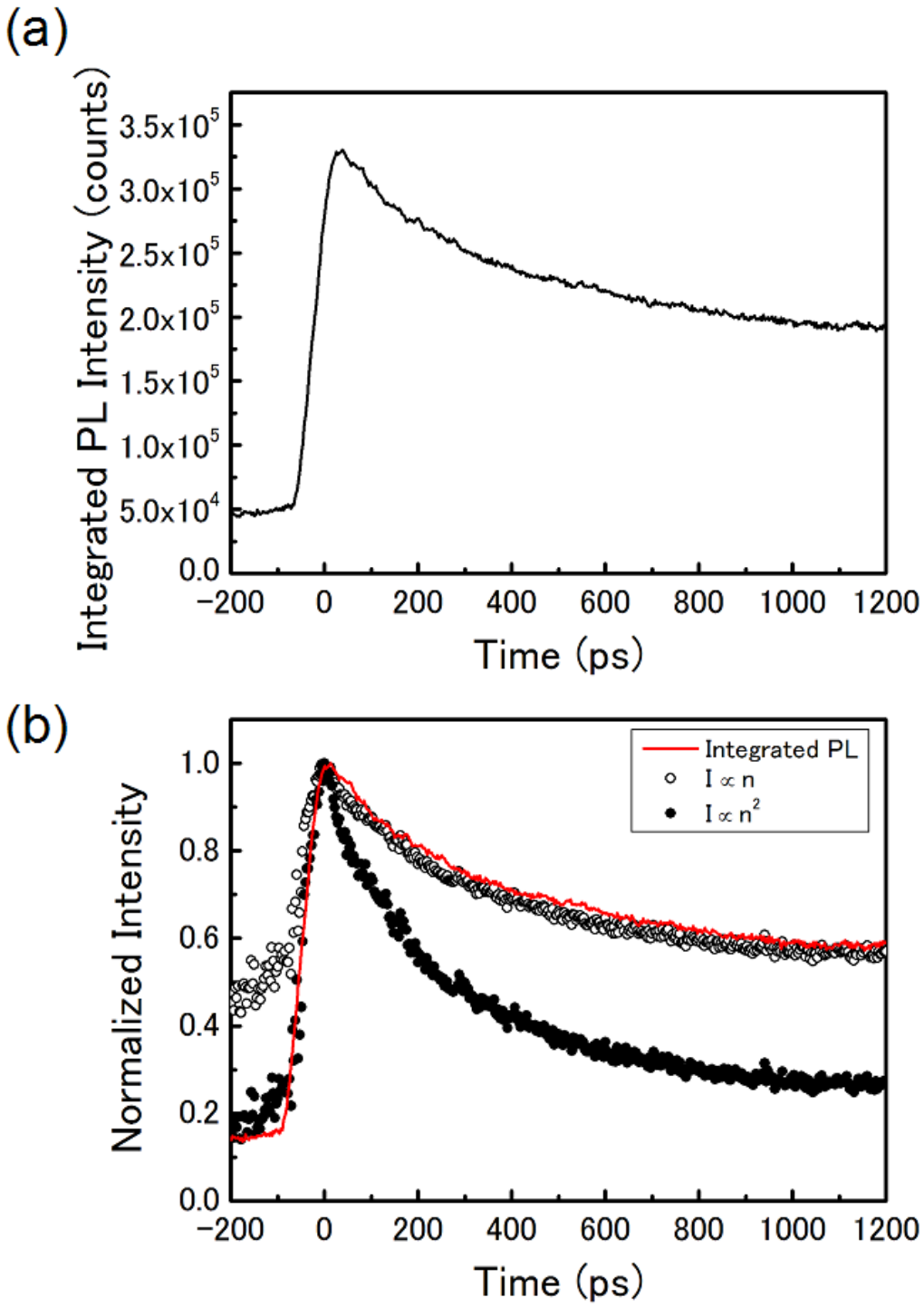

Figure 5.11 (a) Temporal change of the integrated PL intensity. (b) Normalized plots of S_{PL} (solid line), n (open circle), and n^2 (filled circle).

5.4.2 Carrier diffusion

The blue shift caused by the band bending is decided by not the *numbers* of exciton but the *density* of exciton. In other words, the decreasing of a confinement-energy remarkably shows a decrease of the exciton density. We consider a decrease of the exciton density by the exciton diffusion in a CMS-NW. The schematic images of the exciton diffusion in a CMS-NW are shown in **Figure 5.12**. The exciton is excited from the top of the wire at the penetration depth immediately after the excitation. The excitons diffuse into the whole area of the CMS-NW in several hundred picoseconds. Moreover, because the exciton lifetime is very long, we assume that the number of excitons (N) is conserved in the time-domain of several hundred picoseconds. The area where the excitons exist is assumed to be S. Then, the exciton density to represented as $n = N/S$. The PL intensity is calculated as the product of the bimolecular recombination rate proportional to n^2 and the luminescence spectrum area [$S(t)$].

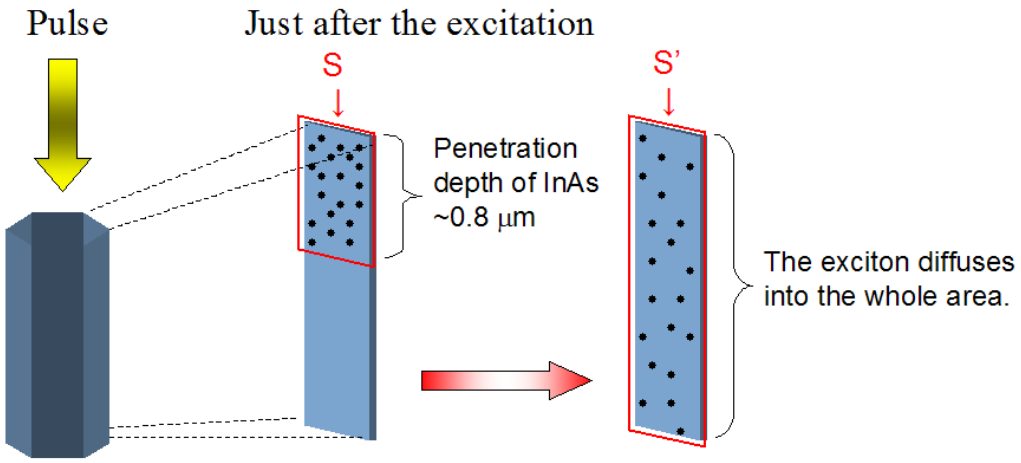

Number of exciton : N

Luminescence area : $S(t)$

Exciton density : $n(t) = N/S(t)$

PL intensity :

$$I(t) \propto n^2(t) \cdot S(t)$$
$$= N \cdot n(t)$$
$$= \frac{N^2}{S(t)}$$

Figure 5.12 The schematic images of the carrier diffusion in a CMS-NW.

$$
\begin{aligned}
I &\propto n^2(t)\cdot S(t) \\
&= \frac{N^2}{S(t)} \\
&= N\cdot n(t)
\end{aligned}
\qquad (5.7)
$$

When the luminescence area doubles, the exciton density and the PL intensity are reduced by half. Therefore, the temporal change of the luminous intensity is proportional to the temporal change of the exciton density, when the area of luminescence increases by the exciton diffusion. This can explain **Figure 5.11 (b)**.

Now, let us evaluate the exciton diffusion by using one-dimensional diffusion equation with a diffusion coefficient of D:

$$
\frac{d\rho(z,t)}{dt} = D\frac{d^2\rho(z,t)}{dz^2} \quad , \qquad (5.8)
$$

where $\rho(z,t)$ is the exciton distribution function at the position z and the time t. Immediately after the excitation, the excitons are distributed as a Gaussian distribution with the half width of the penetration depth ($\lambda_D = 2\sqrt{D\tau}$) for simplicity. The temporal change of the exciton distribution function is described as follows by solving the equation (5.8).

$$
\rho'(z,t) = \frac{1}{2\sqrt{\pi D(t-\tau)}} e^{-\frac{z^2}{4D(t-\tau)}} \quad . \qquad (5.9)
$$

We consider the folding of the exciton density distribution function at both ends of the wire by using the method of images. When the length of the wire is assumed to be l, the exciton distribution by the method of images becomes

$$
\begin{aligned}
\rho(z,t) &= \rho'(z,t) + \rho'(z-2l,t) + \rho'(z+2l,t) + \rho'(z-4l,t) + \cdots \\
&= \sum_{k=0}^{\infty} \rho'(z \pm 2kl, t)
\end{aligned}
\qquad (5.10)
$$

Therefore, the temporal change of the exciton number in the wire is

$$n(t) = \int_0^l \rho(z,t)dx \quad . \qquad (5.11)$$

Schematic image of the method of images is shown in **Figure 5.13**. We calculate equations (5.10) and (5.11) with assuming the diffusion coefficient of $D = 5.17 \times 10^{-4}$ m^2/s. Other parameters are used as follows: $l = 2$ μm and $\lambda_D = 0.8$ μm. **Figure 5.14** shows the results of the model calculation of exciton distribution [$\rho(z,t)$]. We find that the career diffuses to the whole area of the wire with short time evolution. **Figure 5.15** shows a temporal change of exciton density [$n(t)$] calculated by equation (5.11), well fits to the experimental integrated PL intensity and exciton density. A good agreement is obtained between the diffusion model calculation and the experimental results.

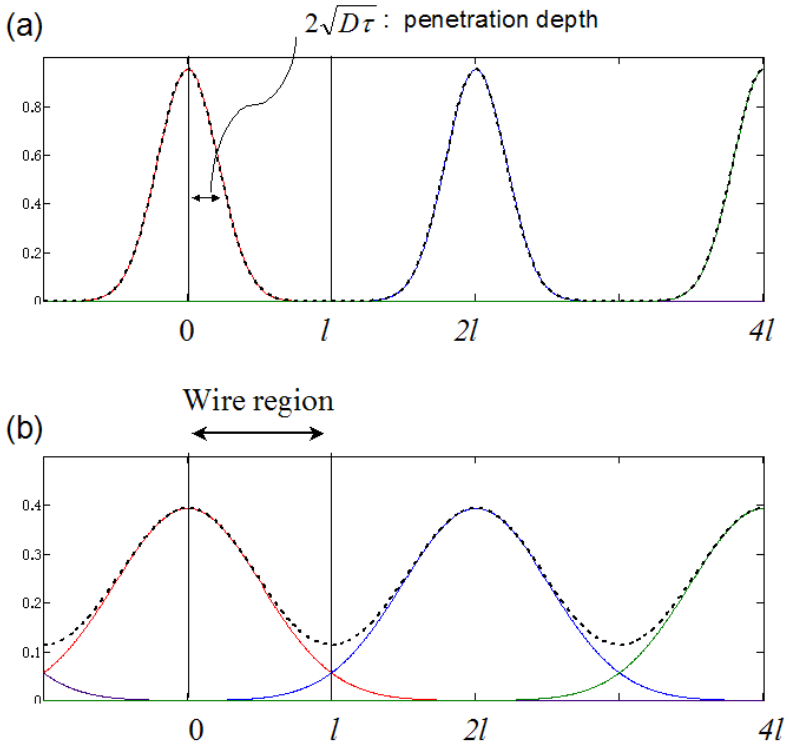

Figure 5.13 Exciton distributions are calculated by the method of images. (a) Just after the excitation. (b) After time proceeds.

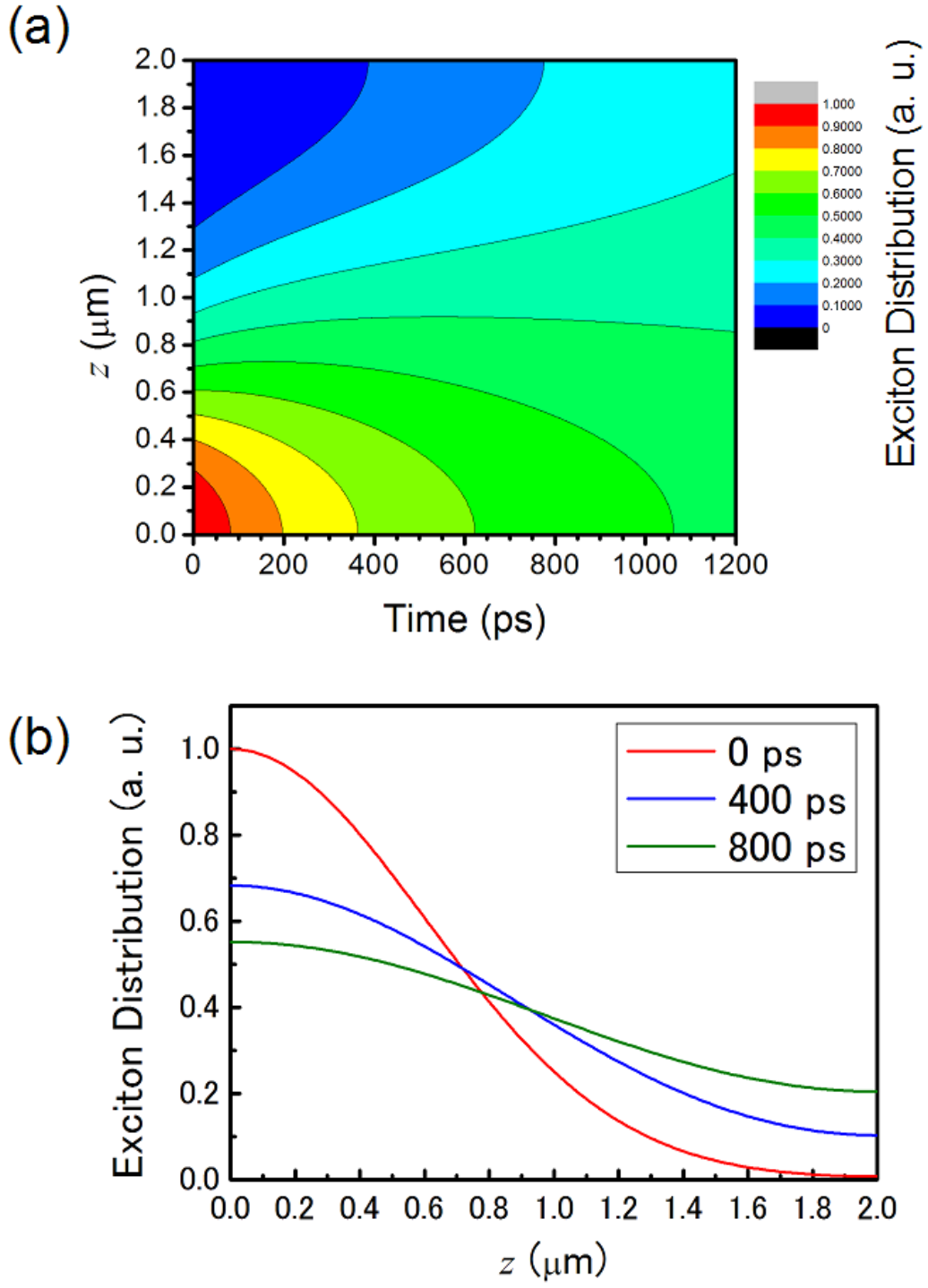

Figure 5.14 (a) Contour map of position- and time-resolved exciton distribution. (b) Carrier distributions at 0, 400, and 800 ps, respectively.

5.5 Summary

Now, we conclude this chapter. The streak measurement shows that the fast decay component appears at the higher energy side of PL band. We consider that this higher energy component originates from the blue shift of the confinement-energy caused by the band bending. The temporal change of a confinement-energy is described by the temporal change of the exciton density. Calculation shows that the decrease in the exciton density is due to not a decrease in the number of excitons by the bimolecular recombination but exciton diffusion. We consider that the initial red shift of a confinement-energy is caused by the exciton diffusion and the resultant relaxation of band bending.

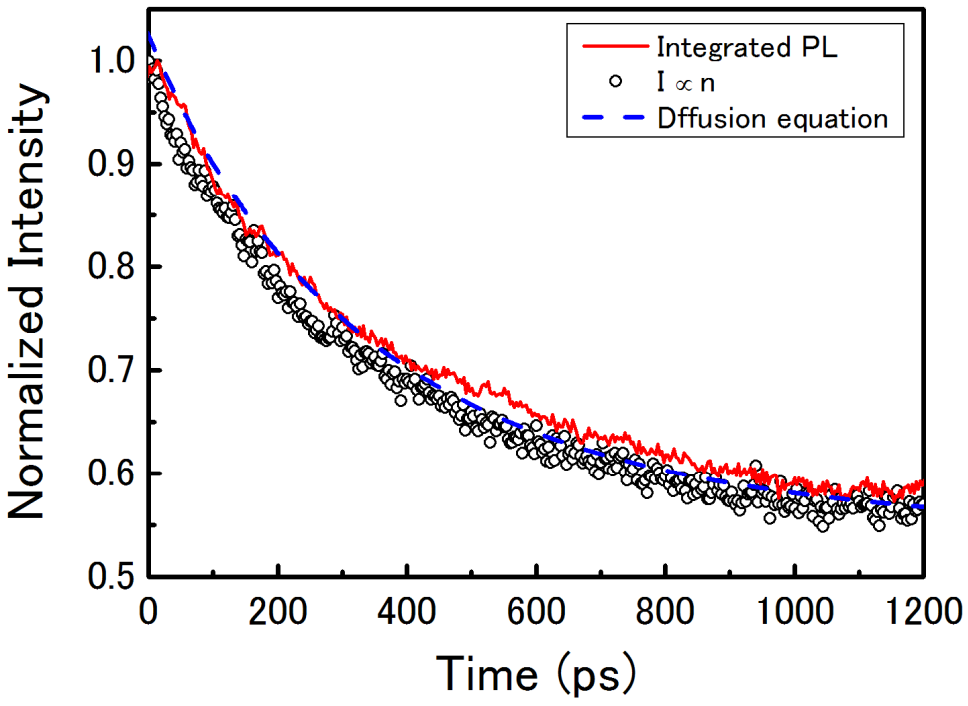

Figure 5.15 The temporal change of calculated exciton density (broken line) fitting to the experimental results of integrated PL intensity (solid line) and exciton density (open circle).

References

[5.1]: N. N. Ledentsov, J. Bohrer, M. Beer, F. Heinrichsdorff, M.Grundmann, D. Bimberg, S. V. Ivanov, B. Ya. Meltser, S. V. Shaposhnikov, I. N. Yassievich, N. N. Faleev, P. S. Kop'ev, and Zh. I. Alferov: Phys. Rev. B. **52**, 14058 (1995).

[5.2]: C. Weisbuch and B. Vinter: *Quantum Semiconductor Structures* (Academic Press, Boston, 1991), p. 20.

[5.3]: H. J. Davies: *Teijigen Handotai no Butsuri* (The physics of low-dimensional semiconductors) (Springer, Tokyo, 2004), p. 364 [in Japanese]

[5.4]: X. D. Luo, C. Y. Hu, Z. Y. Xu, H. L. Luo, Y. Q. Wang, J. N. Wang, and W. K. Ge: Appl. Phys. Lett. **81**, 3795 (2002).

[5.5]: J. Hellara, K. Borgi, H. Maaref, V. Souliere, and Y. Monteil: Mater. Sci. Eng., C **21**, 231 (2002).

[5.6] T. T. Chen, C. L. Cheng, Y. F. Chen, F. Y. Chang, H. H. Lin, C.-T. Wu, and C.-H. Chen: Phys. Rev. B **75**, 033310 (2007).

[5.7]: S. Schmitt–Rink, D. S. Chemla, and D. A. B. Miller: Phys. Rev. B **32**, 6601 (1985).

[5.8]: Y. Masumoto, S. Shionoya, and H. Okamoto: Opt. Commun. **53**, 385 (1985).

Chapter 6.

Conclusion

In summary, photoluminescence (PL) and time-resolved PL spectra from InP/InAs/InP coremultishell nanowires (CMS-NW) are measured. Our study suggests a type-II optical transition in the wurtzite crystal structure due to triaxial compressive strain in these novel nanostructures. The spectral diffusion takes place in two stages depending on the dimensionality of the confinement. This suggests that the photo-excited excitons undergo the first-stage two-dimensional spectral diffusion in the side plane and the second-stage one-dimensional spectral diffusion in the corner line region in the CMS-NW successively. The relaxation of the band bending causes fast PL decay at the higher energy side of the PL band. The relaxation of the transient band bending is reflected by the diffusion-induced decrease of the exciton density. These findings will be important for further progress in the fabrication of the CMS-NW and for the development of nanodevices based on such structures.

Acknowledgements

I would like to appreciate to Prof. Yasuaki Masumoto at University of Tsukuba for many valuable instructions and continuous encouragement.

I would like to acknowledge to Dr. Michio Ikezawa and Dr. Shinichi Tomimoto at University of Tsukuba for their experimental supports and valuable advices. I would like to acknowledge to Dr. Bipul Pal at Indian Institute of Science Education and Research Kolkata for his fruitful discussions and helpful assistance throughout the experiments.

I am deeply grateful to Dr. Premila Mohan, Prof. Junichi Motohisa and Prof. Takashi Fukui at Hokkaido University for preparing high-quality InP/InAs/InP core-multishell nanowire sample.

I wish to thank Prof. Ken-ichi Hino of University at Tsukuba for the executing Fortran program. I gratefully thank to Dr. Shinichi Watanabe at the University of Tokyo for the development of finite element method calculation. I wish to thank Prof. Toshihide Takagahara at Kyoto Institute of Technology for his important advice of the spectral diffusion.

I would like to thank the members of Masumoto Laboratory. I have very good memories with them.

Finally, I would like to thank my family for their loving support.

Appendix. A

Deriving the sheet exciton density in the steady-state

A bimolecular recombination process gives the rate equation of exciton density n described by

$$\frac{dn}{dt} = -\alpha \cdot n^2 + G \quad , \tag{A.1}$$

where G means generation rate of excitons by the photo-excitation proportional to the excitation power density P ($G \propto P$), and α is the bimolecular recombination rate. In the steady-state condition, the exciton density does not vary in time,

$$\frac{dn}{dt} = 0 \quad . \tag{A.2}$$

Then, equation (A.1) is rewritten as

$$\begin{aligned} -\alpha \cdot n^2 + G &= 0 \\ \alpha \cdot n^2 &= G \propto P \\ n^2 &\propto P \end{aligned} \quad . \tag{A.3}$$

Therefore, the exciton density squared is proportional to the excitation power density.

Appendix. B

Estimation of the sheet exciton density

The excitation energy density per pulse (I_{exc}) divided by the excitation energy ($h\nu$) gives the density of photons per pulse (N_p).

$$N_p = \frac{I_{exc}}{h\nu} \quad . \tag{B.1}$$

The horizontal cross-sectional area of the InAs layer for one side of the hexagon is given by $S = a \times l$, where a is the InAs well width and l is the length of the side. Therefore the photon numbers of $N_p \times S$ are illuminating one side plane of the InAs layer from the top of the CMS-NW. We consider the one photon creates the one electron-hole pair forming a type-II exciton. Therefore, $N_p \times S$ excitons are created in the InAs layer from the top of the CMS-NW by the pulse laser. The photo-created excitons areconsidered to be distributed into the penetration depth of d and to be spread within the area of $S' = l \times d$ from the top of the CMS-NW. Therefore the photo-created sheet exciton density (n) are estimated by

$$\begin{aligned} n &= \frac{N_p S}{S'} \\ &= \frac{N_p a}{d} \end{aligned} \quad . \tag{B.2}$$

For example, the exciton density of 3.4×10^{15} m^{-2} is estimated under the excitation condition we used: I_{exc} = 1.2 J/m^2, $h\nu = 2.2 \times 10^{-19}$ J (corresponding to the excitation wavelength of 900 nm), a = 0.5 nm, and d = 800 nm.

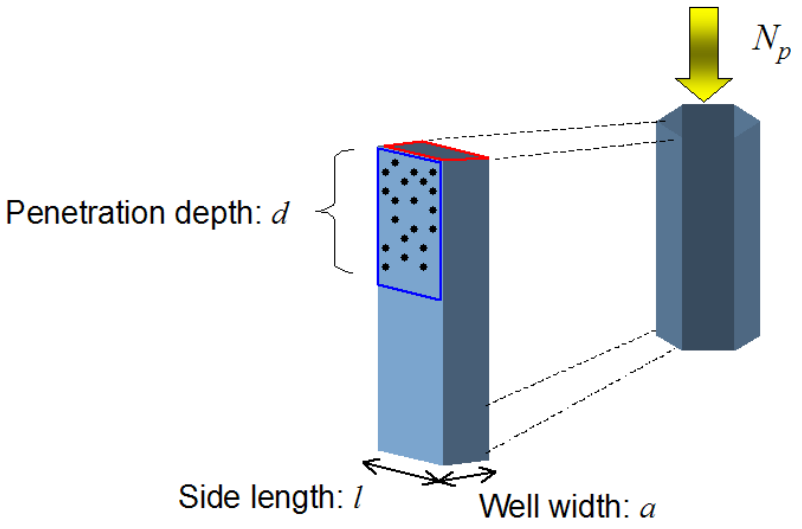

Horizontal cross-sectional area of the InAs layer:	$S = a \times l$
Photo-excited carrier spreading area:	$S' = d \times l$

Figure B.1 Schematic image of estimating the carrier density.

Appendix. C

Exciton-phonon interaction Hamiltonian for both the type-I exciton and the type-II exciton

The spectral diffusion of type-I excitons can be calculated by the three-dimensional exciton-phonon interaction Hamiltonian **[C.1]**. The envelope function of the type-I exciton of the lowest (*1s*) energy can be expressed as **[C.2]**

$$F_{1s}(r_{//}, z_e, z_h) = N_A \phi_{1s}(r_{//}, z_e, z_h)\psi_e(z_e)\psi_h(z_h)$$
$$\psi_n(z_n) = \cos(\pi z_n / L_z) \qquad n : e\ ,\ h \qquad \text{(C.1)}$$

where the center of the well is set as the origin of the *z*-axis, and ϕ_{1s} is a trial function of the *1s* excion,

$$\phi_{1s}(r_{//}, z_e, z_h) = \exp[-\{\alpha^2 r_{//}^2 + \beta^2 (z_e - z_h)^2\}^{1/2}] \qquad \text{(C.2)}$$

On the contrary, the envelope function of the type-II exciton for the *1s* state can be expressed as **[C.3]**

$$F_{1s}(r_{//}, z_e, z_h) = N_A \phi_{1s}(r_{//}, z_e, z_h)\psi_h(z_h)$$
$$\psi_h(z_h) = \sin(\pi z_h / L_z) \qquad , \qquad \text{(C.3)}$$

where the hetero interface is set as the origin of the *z*-axis perpendicular to the QW interface, and ϕ_{1s} is exactly the same as the equation (C.2). Note that $\psi_e(z_e) = 1$, for the electron existing in a barrier layer as the continuous state. N_A is a normalized constant for both the cases. Therefore, the only one difference between the envelope functions of type-I and type-II exciton is in the *z*-axis component.

The three-dimensional electron-phonon interaction Hamiltonian for the deformation-potential coupling is expressed as

$$H_{ex-ph}^{DF} = \sum_{\mathbf{K}_{//},\mathbf{K}'_{//},q_z} \left[\Xi_c(\mathbf{K}'_{//}-\mathbf{K}_{//},q_z)H_\lambda(-\alpha_h(\mathbf{K}_{//}-\mathbf{K}'_{//}),q_z) - \Xi_v(\mathbf{K}'_{//}-\mathbf{K}_{//},q_z)H_\lambda(-\alpha_e(\mathbf{K}_{//}-\mathbf{K}'_{//}),q_z)\right] \left|\lambda,\mathbf{K}'_{//}\right\rangle\left\langle\lambda,\mathbf{K}_{//}\right| (b_{\mathbf{K}'_{//}-\mathbf{K}_{//},q_z} + b^{\dagger}_{\mathbf{K}_{//}-\mathbf{K}'_{//},-q_z}) \qquad \text{(C.4)}$$

with

$$H_\lambda(\mathbf{Q}_{//},Q_z) = \int d^2 r_{//} \int dz_e \int dz_h \left|F_{1s}(\mathbf{r}_{//},z_e,z_h)\right|^2 \exp(iQ_z q_e + i\mathbf{Q}_{//}\cdot\mathbf{r}_{//}) \qquad \text{(C.5)}$$

where $\Xi_{c(v)}$ shows the deformation potential function for the conduction (valence) band coupling with LA-phonon. Equation (C.4) shows that the difference of the deformation-potential between the conduction band and the valance band is the essential part of the interaction Hamiltonian. Equation (C.5) shows that integration of the components parallel to the QW interface ($\mathbf{r}_{//}$) gives the same expression for both the type-I exciton and the type-II exciton, because the same trial function (C.2) is used for both the type-I and type-II exciton. In the case of two-dimensional exciton, the integration of the *z*-axis component, expressed in equation (C.5), becomes constant at the limit where a thickness of the well L_z is zero. Thus the constant can be included in the normalized constant N_A. Summarizing the above mentioned, the essential part of the exciton-phonon interaction Hamiltonian for the deformation-potential coupling has the same expression for both the type-I exciton and the type-II exciton except the normalization constant.

[C.1]: T. Takagahara: Phys. Rev. B. **31**, 6552 (1985).

[C.2]: Y. Shinozuka and M. Matsuura: Phys. Rev. B. **28**, 4878 (1983); Phys. Rev. B. **29**, 3717(Erratum) (1984).

[C.3]: M. Matsuura and Y. Shinozuka: Phys. Rev. B. **38**, 9830 (1988).

List of Publication

[1] ***"Time- and Spectrally-Resolved PL Study of a Regular Array of InP/InAs/InP Core-multishell Nanowires"***
B. Pal, K. Goto, M. Ikezawa, Y. Masumoto, P. Mohan, J. Motohisa, and T. Fukui
Proceedings of the Quantum Electronics and Laser Science Conference 2007. (Baltimore, 2007).

[2] ***"Type-II behavior in wurtzite InP/InAs/InP core-multishell nanowires"***
B. Pal, K. Goto, M. Ikezawa, Y. Masumoto, P. Mohan, J. Motohisa, and T. Fukui
Appl. Phys. Lett. **93**, 073105 (2008).

[3] ***"Spectral diffusion of type-II excitons in wurtzite InP/InAs/InP core-multishell nanowires"***
B. Pal, K. Goto, M. Ikezawa, Y. Masumoto, P. Mohan, J. Motohisa, and T. Fukui
Proceedings of the 15th International Conference on Luminescence and Optical Spectroscopy of Condensed Matter. (Lyon, 2008).

[4] ***"Transient band-bending in InP/InAs/InP core-multishell nanowires"***
K. Goto, B. Pal, S. Tomimoto, Y. Masumoto, P. Mohan, J. Motohisa, and T. Fukui
Phys. status solidi C. **6**, 205 (2009).

[5] ***"One-dimensional and Two-dimensional Spectral Diffusion in InP/InAs/InP Core-Multishell Nanowires"***
K. Goto, M. Ikezawa, S. Tomimoto, B. Pal, Y. Masumoto, P. Mohan, J. Motohisa, and T. Fukui
Jpn. J. Appl. Phys. (2009, to be published)